The University of Alabama in Huntsville

Final Report

THE VARIABLE POLARITY PLASMA ARC WELDING PROCESS: CHARACTERISTICS AND PERFORMANCE

NASA Contract: NAS8-36955/

Delivery Order No. 80

Prepared by

R. J. Hung, and G. J. Zhu

The University of Alabama in Huntsville

Huntsville, Alabama 35899

June 1991

ABSTRACT

Significant advantages of the Variable Polarity Plasma Arc (VPPA) welding process include faster welding, fewer repairs, less joint preparation, reduced weldment distortion, and absence of porosity. The power distribution has been analyzed for an argon plasma gas flow constituting the fluid in the VPPA welding process. The major heat loss at the torch nozzle is convective heat transfer; in the space between the outlet of the nozzle and the workpiece, radiative heat transfer; and in the keyhole in the workpiece, convective heat transfer. The power absorbed at the workpiece produces the molten puddle that solidifies into the weld bead. Crown and root widths, and crown and root heights of the weld bead are predicted. The basis is provided for an algorithm for automatic control of VPPA welding machine parameters to obtain desired weld bead dimensions.

NOMENCLATURE

A_C = Crown reinforcement area (cm^2)

A_E = Cross-sectional area of electrode (cm^2)

A_N = Nozzle circumferential area (cm^2)

A_r = Root reinforcement area (cm^2)

C_p = Constant pressure specific heat ($J/^0K$)

D = Nozzle diameter (cm)

D_E = Electrode diameter (cm)

d_c = Crown bead width (cm)

d_r = Root bead width (cm)

$\frac{dv}{dL}$ = Voltage drop per unit length (V/mm)

d_w = Feed wire diameter (mm)

g = Gravitational acceleration (cm/s^2)

h_c = Crown height (mm)

h_{exit} = Plasma jet enthalpy at the exit of workpiece (J/g)

h_N = Plasma enthalpy corresponding to the nozzle wall temperature (J/g)

h_{plasma} = Plasma enthalpy (J/g)

h_r = Root height

$h_{1,i}$, $h_{1,o}$ = Plasma enthalpy at entrance and exit ends, respectively, of gap between electrode and nozzle

$h_{2,i}$, $h_{2,o}$ = Plasma enthalpy at entrance and exit ends, respectively, of nozzle

$h_{3,i}$, $h_{3,o}$ = Plasma enthalpy at entrance and exit ends, respectively, of standoff column

$h_{4,i}$, $h_{4,o}$ = Plasma enthalpy at entrance and exit ends, respectively, of workpiece keyhole

I_m^+, I_m^- = Main electric current in straight and reverse polarities, respectively

I_p^+, I_p^- = Pilot electric current in straight and reverse polarities, respectively

k = Thermal conductivity of plasma jet

k_E = Thermal conductivity of electrode

L_E = Length of electrode

L_1 = Distance between electrode and nozzle

L_2 = Axial length of nozzle

L_3 = Column distance of standoff

L_4 = Thickness of workpiece

$\dot{m}$ = Argon gas mass flow rate

n = Parabolic exponent of reinforcement shape

$\bar{P}$ = External pressure

P_E = Power input at electrode

$P_{J,1}$ = Joule heating power input in the gap between electrode and nozzle

$P_{J,2}$ = Joule heating power input in the nozzle

$P_{J,3}$ = Joule heating power input in the standoff column

$P_{N,1}$ = Nozzle work function induced power input

$P_{N,2}$ = Nozzle anode and cathode drops induced power input

$P_{W,1}$ = Workpiece work function induced power input

$P_{W,2}$ = Workpiece anode and cathode drops induced power input

$P_{1,i}$, $P_{1,o}$ = Plasma arc power at entrance and exit ends respectively, of gap between electrode and nozzle

$P_{2,i}$, $P_{2,o}$ = Plasma arc power at entrance and exit ends respectively, of nozzle

$P_{3,i}$, $P_{3,o}$ = Plasma arc power at entrance and exit ends respectively, of standoff column

$P_{4,i}$, $P_{4,o}$ = Plasma power at entrance and exit ends, respectively, of workpiece keyhole

Q_{dis} = Plasma arc discharged power loss (at exit end of keyhole)

Q_G = Power loss in the gap between electrode and nozzle

Q_N = Total power loss in the nozzle

$Q_{N,C}$ = Convective heat transfer power loss in the nozzle

$Q_{N,e}$ = Free electron power loss in the nozzle

$Q_{N,G}$ = Direct power loss from the surface of the nozzle contributed by total power input to work function and part of power input to anode and cathode drops at nozzle

Q_s = Standoff column total power loss

Q_w = Total workpiece power loss

$Q_{W,c}$ = Convective heat transfer workpiece power loss

$Q_{w,e}$ = Free electron power loss in the workpiece

R = Nozzle radius

R_i = Distance between heat source and point of computation at workpiece

t_+, t_- = Time duration for straight and reverse polarities, respectively

T_c = Temperature at the point of computation

T_0 = Environment temperature; Initial temperature of workpiece

u = Welding traveling speed

V_A, V_B, V_C, V_D, V_E, V_F, V_G = Straight polarity electric voltage, shown in Figure 1, at points A, B, C, D, E, F, and G, respectively

V_A', V_B', V_C', V_D', V_E', V_F', V_G' = Reverse polarity electric voltage, shown in Figure 1, at points A′, B′, C′, D′, E′, F′, and G′, respectively

$\dot{V}_G$ = Argon plasma volumetric flow rate in the gap between electrode and nozzle

V_s = Argon plasma volume in the standoff column

V_w = Wire feeding speed

W_g = Initial gap distance between two workpieces

y = Coordinate axis

y_c = Axis of coordinate to be used for spatial temperature distribution computation

Z = Coordinate axis

Z_c = Axis of coordinate to be used for spatial temperature distribution computation

$Z_{1\ 35}$ = Heat source spatial point of distribution

α = Angle; workpiece thermal diffusivity

β = Angle

ΔV_a, ΔV_c = Anode and cathode electric potential drops, respectively

ΔV_m^+, ΔV_m^- = Main electric voltage drops in straight and reverse polarities, respectively

ΔV_p^+, ΔV_p^- = Pilot electric voltage drops in straight and reverse polarities, respectively

ϵ_R = Reverse polarity voltage rise

σ = Surface tension coefficient

ϕ = Fraction of heat source distributed in spatial coordinate

ϕ_E = Electrode work function

ϕ_N = Nozzle work function

ϕ_w = Workpiece work function

ψ = Fraction of nozzle, or workpiece, power loss contributed by anode and cathode drops

I. INTRODUCTION

The plasma arc is a concentrated energy source commonly used in welding and cutting processes. It is composed of a partially ionized gas stream produced by forcing an inert gas to flow through an electric arc and emerge from a constricting nozzle. With its high energy density and velocity, the plasma arc, when impinging on the workpiece, can create a hole in the molten pool generated by its heat and can penetrate through the workpiece. Depending on the operating parameters employed, this hole may either become self-healing or remain open as the arc transverses along the workpiece. A "keyhole" welding process occurs in the self-healing case, in which the molten metal in front of the arc flows around the arc column and resolidifies behind the arc. On the other hand, a cutting operation is achieved if the hole remains open (O'Brien, 1968).

The plasma welding process is essentially an extension of gas tungsten-arc welding (GTAW); however, constraining the arc to flow through a nozzle produces much higher energy density in the arc and much higher gas velocity and momentum. The process produces deep penetration welds by forming a keyhole in the workpiece by the pressure of the gas flow. The metal melted in front of the advancing keyhole flows around to the rear where it solidifies to form the weld bead. This is distinct from the essentially surface melting produced by the GTAW process (which cannot normally penetrate to a depth equal to the width of a weld pool).

In 1955 Linde Air Products introduced a plasma arc torch for

metal cutting applications, and by 1965 Linde had developed an automatic plasma arc welding facility for Westinghouse Electric Corporation to fabricate a 120 in. diameter, 3/8 in. thick D6AC steel rocket motor case for the Titan III-C booster assembly (Miller and Filipski, 1966; Privoznik and Miller, 1966). The plasma arc welding process was reported to halve the welding time required. Then in 1965 Thermal Dynamics Corporation reported the use of direct current reversed polarity (workpiece negative) plasma arc to join 1/4 in. thick aluminum plate (Cooper et al., 1965). At the end of the 1960's, Van Cleave at the Boeing Company began his efforts to combine the plasma arc process with a variable polarity feature in which the electrode polarity was periodically reversed. Alternating electrode potential for aluminum welding had been investigated as early as 1947 (Herbst, 1947). Difficulties with welding power supplies in this application were evident early-on. In addition, when variable polarity plasma arc (VPPA) welding was used in the U.S. Army Roland Missile Production Program, development problems such as arc pressure pulsation were noted (Nunes et al., 1981; 1983). As a result of Van Cleave's promising work at Boeing, a VPPA research and development project was initiated in 1978 at the NASA Marshall Space Flight Center, to determine the potential for replacing the GTAW system used in the fabrication of the Space Shuttle External Tank (ET). After the original used in the fabrication and process were improved, VPPA welding finally exceeded the expectations (Nunes et al., 1984a; 1984b).

The Space Shuttle ET (diameter 28.6 ft., length 154 ft.) is the

largest known "drop tank," carrying 140,000 gallons of liquid oxygen and 380,000 gallons of liquid hydrogen. From the outset of ET production, the conventional GTAW system operating in the direct current electrode negative mode was used. With the GTAW system, in spite of the requisite careful joint preparation, weld porosity and defects had been ever-present problems since the fabrication of the Saturn lunar rocket first stage. Therefore, the decision was made at the outset to use 100% radiographic inspection. Weld porosity and defects had to be ground out and repaired systematically.

The VPPA process significantly reduced porosity and defects with less stringent joint preparation and, in addition, reduced weldment distortion, and speeded up the welding process.

In this study, the power distribution for an argon plasma gas has been analyzed along its course through the VPPA welding system. The study includes the following sections:

(1) Electric potential and current distributions of pilot arc and main arc circuits during straight and reverse polarity processes of VPPA welding system operations;

(2) Electric power input at electrode, power input in the gap between electrode and nozzle, power input within the nozzle, power input in the free plasma jet column of standoff, and power input in the keyhole of workpiece;

(3) Thermal power loss in the VPPA welding system including electrode heat conduction loss; heat radiation loss within the gap between electrode and nozzle; power loss within the nozzle which contains heat convection loss within the

nozzle, direct power loss from the surface of the nozzle, and electron collision power loss within the nozzle; power loss in the standoff column; workpiece power loss which contains convective heat loss in the workpiece, direct power loss from the surface of the keyhole, and electron collision power loss in the keyhole; and power discharge loss;

(4) Plasma arc enthalpy of various sections of VPPA welding system including plasma arc enthalpy within the gap between electrode and nozzle, plasma arc enthalpy within the nozzle, plasma arc enthalpy within the standoff column, plasma arc enthalpy within the keyhole of the workpiece, and plasma arc enthalpy discharged from the workpiece;

(5) Prediction of crown and root bead widths of welding;

(6) Prediction of crown and root heights of welding.

II. VARIABLE POLARITY PLASMA ARC WELDING SYSTEM ELECTRIC POTENTIAL CALCULATION

The significant current carriers in a welding arc are electrons and positive ions. Electrons carry the bulk of the current, moving rapidly from negative cathode to positive anode. The positive ions drift more slowly through the interelectrode space. In a fixed polarity arrangement, the differential drift rate results in an asymmetrical heating of the welding arc's ends. The cathode receives less heat and the anode more heat. The straight polarity mode of operation entails a negative electrode (cathode) and a positive workpiece (anode). Where the primary object of the weld process is to deliver the maximum heat to the workpiece with minimum deterioration of the electrode, straight polarity is used.

Reverse polarity, which entails positive electrode and negative workpiece, has the advantage that the workpiece is subjected to a cleaning process (cathodic cleaning) by the impingement of positive ions on the workpiece surface. Recent work suggests that heavy positive ion weight is irrelevant to cleaning process which seems to be more like capacitor breakdown than hammer impact. In the case of plasma arc welding, reverse polarity action appears to condition the surface of the aluminum alloy so that the molten metal flows easily and controllable under the arc. It is conjectured that this fluid control is accomplished through breaking up of surface oxide films. Cutoff of reverse polarity during VPPA welding transforms a weld metal flow which closes smoothly and soundly behind the keyhold to an

irregular, intermittent, globular flow. This process leaves a rough, lumpy bead sunken below the parent metal surface and protruding jaggedly from the root of the weld. However, continuous reverse polarity is not necessary to provide adequate cathodic cleaning action.

The variable polarity square-wave with unequal straight and reverse polarity time intervals offered a combination of the high heating capability of straight polarity with the cleaning feature of reverse polarity. Adequate cleaning is obtained by incorporating a relatively short (1/10 to 1/5 the duration of the straight polarity current) pulse of reverse polarity current into the welding current waveform.

Figure 1 show the VPPA electric power system. During the straight polarity mode of operation, it employs a negative electrode (cathode) and a positive workpiece (anode); during the reverse polarity mode of operation it employs a positive electrode and a negative workpiece. Figure 1 at left illustrates the straight polarity mode; at right, reverse polarity mode.

In electric potential calculation, one has to consider electrode, nozzle and workpiece work functions; anode and cathode drops; electric potential intensity, etc. In reverse polarity, in addition to those considered earlier, one has to consider extra electric potential rise to compensate the thermionic emission in metal workpiece which is very much similar to the extra cathode drop. Following these logics, calculation of electric potential can be obtained from the following formulations:

(A) For Straight Polarity

In straight polarity, electron streams flow from plasma arc to workpiece (anode). Summation of workpiece work function and anode drop is balanced by the electric potential difference between anode potential V_F and plasma arc potential V_E, i.e.,

$$V_F - V_E = \Delta V_a + \phi_W$$

or

$$V_E = V_F - \Delta V_a - \phi_W$$

It is grounded at point F which implies that $V_F = 0$.

Electron traveling distance between points E and C is $L_2 + L_3$ which means that electric potential difference between these two points along the direction of electron flow is

$$V_E - V_C = \frac{dV}{dL} (L_2 + L_3)$$

or

$$V_C = V_E - \frac{dV}{dL} (L_2 + L_3)$$

Similarly, electric potential difference between V_D and V_C resemble to the electric potential difference between V_F and V_E, shown earlier, which is

$$V_D - V_C = \Delta V_a + \phi_N$$

or

$$V_D = V_C + \Delta V_a + \phi_N$$

Electric potential difference between V_C and V_B also resembles to the electric potential difference between V_E and V_C, namely,

$$V_C - V_B = \frac{dV}{dL} L_1$$

$$V_B = V_C - \frac{dV}{dL} L_1$$

Electric potential difference between cathode electric potential V_A and the neighborhood plasma arc potential V_B, $V_A - V_B$ is balanced by the electrode work function and negative cathode drop, i.e.,

$$V_A - V_B = \phi_E - \Delta V_C$$

or

$$V_A = V_B - \Delta V_C + \phi_E$$

The total potential drop in main arc ΔV_m^+ is $V_F - V_A = - V_A$. Thus,

$$\Delta V_m^+ = - V_A$$

The pilot arc potential drop ΔV_p^+ is $V_D - V_A$, i.e.,

$$\Delta V_p^+ = V_D - V_A$$

where ϕ_E = Electrode Work Function

ϕ_N = Nozzle Work Function

ϕ_w = Workpiece Work Function

ΔV_a = Anode Drop

ΔV_C = Cathode Drop

$\frac{dV}{dL}$ = Electric Potential Intensity

(B) For Reverse Polarity

In reverse polarity, similar calculation can be accomplished for solving the electric potential differences. To give an example, the electric potential difference between cathode electric potential V_F'

and the neighborhood plasma arc potential V_E' resembles to the electric potential difference between V_A and V_B in straight polarity, in addition to the consideration of extra reverse polarity rise, ϵ_R, to be used to compensate the thermionic emission loss in workpiece metal (#2219 Aluminum), namely

$$V_E' = V_F' - \phi_W + \Delta V_C + \epsilon_R$$

In this study, mathematical expression based on Nunes (1991a) has been adopted, i.e.,

$$\epsilon_R = \text{Reverse Polarity Rise} = 8 + 20 \frac{t_-}{t_+ + t_+}$$

The rest of the mathematical expressions of electric potential differences in reverse polarity can follow the similar logics shown in the calculation of straight polarity. These mathematical expressions are shown as follows:

$$V_C' = V_E' + \frac{dV}{dL}(L_2 + L_3)$$

$$V_D' = V_C' - \frac{dV}{dL} L_2 + \Delta V_a + \phi_N$$

$$V_B' = V_C' + \frac{dV}{dL} L_1$$

$$V_A' = V_B' + \Delta V_a + \phi_E$$

$$\Delta V_m^- = \Delta V_{A'F'} = V_{A'} - V_{F'} = V_{A'}$$

$$\Delta V_p^- = \Delta V_{A'D'} = V_{D'} - V_{A'}$$

where t_+ = Straight Polarity Time Period

t_- = Reverse Polarity Time Period

III. VPPA Welding System Electric Power Input

The pilot arc current, superimposed upon the main arc current between the electrode and the plasma nozzle, comes from a separate power supply located in the plasma control console. The pilot arc polarity does not alternate. The nozzle is held positive with respect to the electrode so that the electron flow is always away from the electrode toward the nozzle. The main arc is started by applying high frequency alternating voltage between the electrode and the plasma nozzle so as first to establish the pilot arc from which the main arc proceeds. The high frequency current is controlled by the plasma control console, but is generated by the spark gap oscillator located in the hot block.

The total electric power input of the VPPA welding system includes the pilot arc between electrode and nozzle as well as the main power arc between electrode and workpiece during the straight polarity and reverse polarity modes. VPPA Electric Power Input can be calculated as follows:

$$P_{total} = \frac{I_m^{+}\Delta V_m^{+}t_{+} + I_p^{+}\Delta V_p^{+}t_{+} + I_m^{-}\Delta V_m^{-}t_{-} + I_p^{-}\Delta V_p^{-}t_{-}}{t_{+} + t_{-}} \qquad (3\text{-}1)$$

where I_m^{+} = Straight Polarity Main Current

I_p^{+} = Straight Polarity Pilot Current

I_m^{-} = Reverse Polarity Main Current

I_p^{-} = Reverse Polarity Pilot Current

Equation (3-1) is the total electric power input of the system which is the summation of power input for the plasma arc jet in the gap between

electrode and nozzle, power input within nozzle, power input in free jet column (standoff), and power input within keyhole of workpiece. These power input can be itemized, and calculated as follows:

(III-A) Power Input at the Electrode

$$P_E = \frac{(I_m^+ + I_p^+)(\Delta V_C - \phi_E)t_+ + (I_m^- - I_p^-)(\Delta V_a - \phi_E)t_-}{t_+ + t_-} \qquad (3\text{-}2)$$

(III-B) Power Input in the Gap Between Electrode and Nozzle (Joule Heating)

$$P_{J,1} = \frac{(I_m^+ + I_p^+)\left(\frac{dV}{dL} L_1\right)t_+ + (I_m^- - I_p^-)\left(\frac{dV}{dL} L_1\right)t_-}{t_+ + t_-} \qquad (3\text{-}3)$$

(III-C) Power Input Within Nozzle

This includes power input through the work function of metal

$$P_{N,1} = \frac{I_p^+ \phi_N t_+ + I_p^- \phi_N t_-}{t_+ + t_-} \qquad (3\text{-}4)$$

Power input through anode and cathode drops,

$$P_{N,2} = \frac{I_p^+ \Delta V_a t_+ + I_p^- \Delta V_a t_-}{t_+ + t_-} \qquad (3\text{-}5)$$

and power input through Joule heating of nozzle

$$P_{J,2} = \frac{I_m^+ \left(\frac{dV}{dL}\right) L_2 t_+ + (I_m^- - I_p^-)\left(\frac{dV}{dL}\right) L_2 t_-}{t_+ + t_-} \qquad (3\text{-}6)$$

(III-D) Power Input in the Free Plasma Jet Column (Standoff) (Joule Heating)

$$P_{J,3} = \frac{I_m^+ \left(\frac{dV}{dL}\right) L_3 t_+ + I_m^- \left(\frac{dV}{dL}\right) L_3 t_-}{t_+ + t_-} \qquad (3\text{-}7)$$

(III-E) Power Input in the Keyhole of Workpiece

This includes power input through the work function of metal and reverse polarity potential rise

$$P_{w,1} = \frac{I_m^+ \phi_w t_+ + I_m^- (\epsilon_R - \phi_w) t_-}{t_+ + t_-} \qquad (3\text{-}8a)$$

and power input through anode and cathode drops

$$P_{w,2} = \frac{I_m^+ \Delta V_a t_+ + I_m^- \Delta V_c t_-}{t_+ + t_-} \qquad (3\text{-}8b)$$

(II-F) Total Power Input of VPPA Welding System

Total power input of VPPA welding system, shown in Equation (3-1) is equal to the summation of power input shown in Equation (3-2) to (3-8), namely

$$P_{total} = P_E + P_{J,1} + P_{N,1} + P_{N,2} + P_{J,2} + P_{J,3} + P_{w,1} + P_{w,2} \qquad (3\text{-}9)$$

IV. Power Loss Calculation of VPPA Welding System

Power loss of VPPA system includes (a) electrode heat conduction loss, (b) heat radiation loss within the gap between the electrode and the nozzle, (c) power loss within the nozzle which contains heat convection loss within the nozzle, direct power loss from the surface of the nozzle, and electron collision power loss within the nozzle, (d) power loss in the standoff column, (e) workpiece power loss which includes convective heat loss in the workpiece, direct power loss from the surface of the keyhole, and electron collision power loss in the keyhole, and (f) power discharge loss. These power losses of VPPA welding system are itemized and are illustrated as follows:

(IV-A) Electrode Heat Conduction Loss

One-dimensional formulation of electrode heat conduction loss is used. The equation is given by

$$Q_E = k_E \cdot A_E \frac{(T_E - T_0)}{L_E} \qquad (4\text{-}1)$$

where

Q_E = Electrode Heat Conduction Loss

k_E = Thermal Conductivity Coefficient of Electrode

A_E = Cross-sectional Area of Electrode

L_E = Length of Electrode

$T_E - T_0$ = Temperature Difference between Ends of Electrode

(IV-B) Heat Radiation Loss Within the Gap Between Electrode and Nozzle

Plasma arc heat radiation loss within the gap between electrode

and nozzle can be computed from the following equation (Evans and Tankin, 1967; Cram, 1985; and Nunes, 1991b):

$$Q_G(W) = V_G(m^3)(4 \times 10^{10})\left[\frac{T(^0K)}{15000}\right]^{16} \Big/ \left\{1 + \left[\frac{T(^0K)}{15000}\right]^{16}\right\} \qquad (4\text{-}2)$$

where

Q_G = Heat Radiation Loss Within the Gap Between Electrode and Nozzle (W)

V_G = Plasma Arc Jet Volume Within Gap Between Electrode and Nozzle (m^3)

T = Average Enthalpy of Plasma Arc Jet Corresponding Temperature (^0K)

(IV-C) Power Loss Within the Nozzle

Power Loss within the nozzle is comprised in the following items:

(IV-C-1) Heat Convection Loss Within the Nozzle

Heat convection loss within the nozzle can be computed from the following formulation of convective heat transfer model (Hsu and Rubinsky, 1987):

$$Nu = 0.2233(X^+)^{-0.7455} + 3.66 \qquad (4\text{-}3)$$

where

$$X^+ = \frac{X}{R} \cdot \frac{1}{(Re \cdot Pr)_m}$$

Here

X = Axial Distance, half size of nozzle length is used for calculation

R = Radius of Nozzle

Re = Reynolds Number of Plasma

Pr = Prandtl Number of Plasma

Nu = Nusselt Number of Plasma

Subscript m = mean values

Heat convection loss within the nozzle, thus, can be computed from the Nusselt number obtained from Equation (4-3), namely,

$$Q_{N,c} = Nu \cdot A_N \cdot \frac{k}{D} \cdot \frac{(h_{plasma} - h_N)}{c_p} \qquad (4-4)$$

where

$Q_{N,c}$ = Heat Convection Loss within the Nozzle

A_N = Heat Transfer Area of Nozzle

D = Diameter of Nozzle

k = Thermal Conductivity of Plasma Arc

c_p = Constant Pressure Specific Heat of Plasma Arc

h_{plasma} = Average Enthalpy of Plasma Arc through the Nozzle

h_N = Average Enthalpy of Nozzle corresponding to the Nozzle Wall Temperature

All thermal properties of physical parameters used in this model shall be checked from the temperature corresponding to the average enthalpy of plasma arc.

(IV-C-2) Direct Power Loss from the Surface of Nozzle

Direct power loss from the nozzle surface includes $P_{N,1}$, nozzle work function induced power input; and part of $P_{N,2}$, nozzle anode and cathode drops induced power input, namely

$$Q_{N,G} = P_{N,1} + \phi P_{N,2} \qquad (4-5)$$

where,

$Q_{N,G}$ = Direct power loss from the nozzle surface

ψ = Fraction of nozzle power loss contributed by anode and cathode drops

$(1-\psi)P_{N,2}$ = Plasma arc power input contributed by nozzle anode and cathode drops

(IV-C-3) Electron Collision Power Loss Within Nozzle

Power loss conducted into nozzle by free electrons can be calculated from the following equation:

$$Q_{N,e} = \frac{I_p}{e}\left(\frac{3}{2}KT\right) \qquad (4\text{-}6)$$

where

$Q_{N,e}$ = Free electron power loss in the nozzle

e = Electron charge = 1.602×10^{-19} coulomb/mole

K = Boltzman constant = 1.38×10^{-16} erg/mol·K

T = Plasma temperature of electrons entering nozzle, approximately; and I_p is the mean pilot current which can be computed as follows:

$$I_p = \frac{I_p^{+}t_{+} + I_p^{-}t_{-}}{t_{+} + t_{-}} \qquad (4\text{-}7)$$

Total power loss in nozzle, Q_N, is the summation of Equations (4-4), (4-5), and (4-6), namely,

$$Q_N = Q_{N,c} + Q_{N,G} + Q_{N,e} \qquad (4\text{-}8)$$

(IV-D) Power Loss in the Standoff Column

Power loss in the standoff column includes radiative heat loss, $Q_{s,r}$, and convective heat loss, $Q_{s,c}$.

Calculation of radiative heat loss is similar to Equation (4-2) for that in the gap between electrode and nozzle, namely

$$Q_{s,r}(W) = V_s(m^3)(4 \times 10^{10})\left[\frac{T(^0K)}{15000}\right]^{16} \Big/ \left\{1 + \left[\frac{T(^0K)}{15000}\right]^{16}\right\} \qquad (4\text{-}9)$$

where V_s denotes plasma arc volume within the standoff column; and T is the temperature corresponding to the average value of plasma arc enthalpy.

(IV-E) Total Workpiece Power Loss

The shape of plasma contact areas in the keyhole of the workpiece is taken to resemble a finger ring. Computations yield a heat transfer rate out of rear half of a keyhole rather than that of the front half. This ring-shaped geometry can be simplified and expanded as illustrated in Figure 2.

The keyhole surface has been divided into 5 equal segments along the keyhole axis between the inlet and outlet ends. Figure 2 shows the geometrical parameters of the segment. Effective heat transfer areas of the keyhole can be computed as follows:

$$L = L_4/5$$

$$a_1 = \pi r$$

$$\alpha^0 = \tan^{-1}\left(\frac{1}{\frac{2}{\pi} - r}\right) = \tan^{-1}\left(\frac{L_4}{\pi r}\right)$$

$$a_2 = a_1 + 2\,\frac{L}{\tan\,\alpha^0}$$

$$A_1 = A_5 = \frac{1}{2}(a_1 + a_2)L = \left(\pi r + \frac{L}{\tan\,\alpha^0}\right)L$$

$$A_2 = A_4 = \left(a_1 + 2\,\frac{L}{\tan\,\alpha^0}\right)L$$

$$= \left(\pi r + \frac{2L}{\tan \alpha^0}\right) L$$

$$A_3 = \left(2\pi r - \frac{L}{\tan \alpha^0}\right) L$$

where

r = Radius of keyhole

L_4 = Thickness of workpiece

and A_1, A_2, A_3, A_4 and A_5 denote effective heat transfer areas of keyhole at Segments 1, 2, 3, 4, and 5, respectively.

Total power loss in the workpiece is comprised in the following items:

(IV-E-1) Convective Heat Loss in Workpiece

Governing equation is same as Equation (4-3), used in nozzle, which is

$$Nu = 0.2233(x^+)^{-0.7455} + 3.66 \qquad (4\text{-}10)$$

where

$$x^+ = \frac{x}{R} \frac{1}{(Re \cdot Pr)_m}$$

Here x is the half thickness of workpiece to be used as the distance for calculation, and the rest of symbols stand for the same meaning as that used in the nozzle.

Heat convection loss in the workpiece can be computed from the Nusselt number obtained from Equation (4-10), namely,

$$Q_{W,c} = Nu \cdot A_w \cdot \frac{k}{D} \frac{(h_{plasma} - h_w)}{c_p} \qquad (4\text{-}11)$$

where A_w stands for heat transfer area of workpiece which is the shape

of plasma contact area in the keyhole and is taken to resemble a finger ring (see Figure 2 for details); and D is the diameter of keyholes which is also the diameter of nozzle if plasma arc jet disperse through standoff column is small enough to be neglected. The rest of symbols are the same as that used in the nozzle.

(IV-E-2) Direct Power Loss from the Surface of Keyhole

Direct power loss from the keyhole surface includes $P_{w,1}$, workpiece work function induced power input; and part of $P_{w,2}$, workpiece anode and cathode drops induced power input, namely

$$Q_{w,G} = P_{w,1} + \psi P_{w,2} \qquad (4\text{-}12)$$

where

$Q_{w,G}$ = Direct power loss from the nozzle surface

ψ = Fraction of workpiece power loss contributed by anode and cathode drops

$(1-\psi)P_{w,2}$ = Plasma arc power input contributed by workpiece anode and cathode drops

In the present model, it is assumed that $\psi = 0$. This is based on the assumption that both anode and cathode drops occur in the plasma flow. Power loss generated by anode and cathode drops are thus absorbed by the plasma flow which raises up the average enthalpy of plasma jet. This higher value of plasma jet enthalpy is then transferred to the workpiece through the convective heat transfer.

In this calculation, the plasma flow parameters used in the model are all one-dimensional. This means that the plasma flow parameters, such as power loss, enthalpy and temperature vary with respect to the axial coordinate of flow direction, while the average values are taken

for all parameters transverse to the flow direction. This assumption matches the concepts described earlier.

(IV-E-3) Electron Collision Power Loss in Keyhole

Power loss due to free electron collision on the surface of keyhole can be calculated from the following equation:

$$Q_{w,e} = \frac{I_m}{e}\left(\frac{3}{2}KT\right) \tag{4-13}$$

where $Q_{w,e}$ denotes free electron power loss in keyhole; T, the average temperature between plasma arc and wall of keyhole; and I_m, the electric current which can be computed from the following equation:

$$I_m = \frac{I_m{}^{+}t_{+}}{t_{+} + t_{-}} \tag{4-14}$$

Thus, total power loss in workpiece, Q_w, is the summation of Equations (4-11), (4-12), and (4-13), namely

$$Q_w = Q_{w,c} + Q_{w,G} + Q_{w,e} \tag{4-15}$$

(IV-F) Power Discharge Loss

Amount of power loss carried away by the plasma jet discharge from the exit end of keyhole, Q_{dis}, can be computed from the plasma arc enthalpy, h_{exit}, multiplied by the mass flow rate of argon gas, m, namely

$$Q_{dis} = h_{exit} \cdot \dot{m} \tag{4-16}$$

Obviously, summation of power loss throughout the entire VPPA welding system is equivalent to the total power input of the system, P_{total}, namely

$$P_{total} = Q_E + Q_G + Q_N + Q_S + Q_W + Q_{dis} \tag{4-17}$$

Calculation of power loss at each part of VPPA welding system

will be illustrated in Section VIII of this report.

V. Calculation of Plasma Arc Enthalpy

Density of argon gas at the pressure of 1 atmosphere and temperature of 298 ^{0}K is

$$\rho_{Ar} = \frac{PM_{Ar}}{R_0 T} = \frac{101320\ (N/m^2) \cdot 39.95\ (kg/kmol)}{8315\ (N \cdot m/kmol - {}^{0}K) \cdot 298\ ({}^{0}K)}$$

$$= 1.6336\ (kg/m^3)$$

where

P = Atmospheric pressure

M_{Ar} = Molecular weight of argon

R_0 = Universal gas constant

T = Temperature

Mass flow rate of argon gas in terms of volumetric flow rate can be shown as

$$\dot{m} = (\dot{V}\ ft^3/hr)\left(\frac{1}{3600}\ hr/s\right)\left(\frac{1}{35.3147}\ m^3/ft^3\right)\rho_{Ar}$$

$$= \frac{1.6336}{(3600)(35.3147)}\ (\dot{V}\ ft^3/hr)$$

$$= 1.285 \cdot 10^{-5}\ (\dot{V}\ ft^3/hr) \qquad (kg/s)$$

$$= 1.285 \cdot 10^{-2}\ (\dot{V}\ ft^3/hr) \qquad (g/s)$$

A shielding gas is needed to isolate the welding system from the surrounding environment. Shielding gas purity is an essential factor in achieving quality welds in any gas shielded arc welding process. The problem of impurities, when manifest, is normally resolved by eliminating the source of the contamination. However, if the gas

supply itself is contaminated, serious schedule interruptions can result, particularly where large manifold gas distribution systems are employed.

Gas contamination affects VPPA welding in several ways. Inside the torch (standoff column), oxygen from water vapor decomposed in the arc can produce a visible oxide film stain on the tungsten electrode. The plasma jet may sputter and exhibit a green coloration from copper eroded from the nozzle under erratic flow conditions. The weld itself may exhibit a packed-looking surface, presumed to be fine porosity due to hydrogen gas from decomposed water vapor. Under severe conditions, the torch may leave behind it a train of irregularities and holes in the weld bead.

Plasma arc power distribution in the whole VPPA welding system can be divided into the following five parts for convenience of discussion: (a) Plasma arc power within the gap between electrode and nozzle, (b) plasma arc power within nozzle, (c) plasma arc power within standoff column, (c) plasma arc power within keyhole of workpiece, and (d) plasma arc power discharged from the workpiece. The plasma arc power associated with ionized argon gases is characterized by the thermal energy parameter enthalpy, which is a function of temperature. The relationship between enthalpy and temperature is non-linear for high temperatures as encountered in the plasma. For these computations the plasma enthalpy-temperature relation is obtained from the tables for argon computed by Drellishak et al. (1963). Thermal properties and transport coefficients of argon plasma are also a function of temperature. The high

temperature argon gas transport coefficients can be obtained from Lancaster (1986), Metcalfe and Quigley (1975), etc. As to aluminum as the workpiece for the present study, the thermal properties can be obtained from American Society for Metals Handbook Committee (1979).

The itemized calculation of plasma arc enthalpy at various sections of VPPA welding system are illustrated as follows:

(V-A) Plasma Arc Enthalpy Within the Gap Between Electrode and Nozzle

Let us assume that entrance and exit ends of plasma arc enthalpy in the gap between electrode and nozzle are $h_{1,i}$ and $h_{1,o}$, respectively.

The plasma arc power at the entrance end of the gap, $P_{1,i}$, is power input at electrode, P_E, subtracting electrode heat conduction loss, Q_E, namely

$$P_{1,i} = P_E - Q_E \tag{5-1}$$

Plasma arc enthalpy at entrance end of the gap, thus, can be calculated as

$$h_{1,i} = \frac{P_{1,i}}{\dot{m}} \tag{5-2}$$

The plasma arc power at the exit end of the gap, $P_{1,o}$, absorbs power through Joule heating, $P_{J,1}$, and gives away power through radiative heat loss, Q_G. It gives

$$P_{1,o} = P_{1,i} + P_{J,1} - Q_G \tag{5-3}$$

Thus, plasma arc enthalpy at exit end of the gap can be calculated from the expression

$$h_{1,o} = \frac{P_{1,o}}{\dot{m}} \qquad (5\text{-}4)$$

(V-B) Plasma Arc Enthalpy Within Nozzle

Let us assume that the plasma enthalpy at the entrance and exit of the nozzle are $h_{2,i}$ and $h_{2,o}$, respectively.

The plasma arc power, $P_{2,i}$, and enthalpy, $h_{2,i}$, at the entrance the nozzle are identical to the plasma arc power, $P_{1,o}$ and enthalpy, $h_{1,o}$ at the exit end of the gap between electrode and nozzle, respectively. Thus

$$\left.\begin{aligned} P_{2,i} &= P_{1,o} \\ h_{2,i} &= h_{1,o} \end{aligned}\right\} \qquad (5\text{-}5)$$

Plasma arc power at the exit end of nozzle, $P_{2,o}$, absorbs power from partial contribution made by nozzle anode drop, $(1-\psi)P_{N,2}$, and full contribution made by Joule heating within nozzle, $P_{J,2}$, and subtracts convective heat loss in nozzle, $Q_{N,c}$, and free electron power loss in nozzle, $Q_{N,e}$. Thus,

$$P_{2,o} = P_{2,i} + (1-\psi)P_{N,2} + P_{J,2} - Q_{N,c} - Q_{N,e} \qquad (5\text{-}6)$$

The corresponding plasma arc enthalpy at the exit end of nozzle is

$$h_{2,o} = \frac{P_{2,o}}{\dot{m}} \qquad (5\text{-}7)$$

(V-C) Plasma Arc Enthalpy Within Standoff Column

Let us assume that entrance and exit ends of plasma arc enthalpy in the standoff column are $h_{3,i}$ and $h_{3,o}$, respectively.

The plasma arc power, $P_{3,i}$, and enthalpy, $h_{3,i}$, at the entrance end of standoff column are identical to the plasma arc power, $P_{2,o}$, and enthalpy, $h_{2,o}$, at the exit end of nozzle, respectively. Thus,

$$\left.\begin{aligned} P_{3,i} &= P_{2,o} \\ h_{3,i} &= h_{2,o} \end{aligned}\right\} \qquad (5\text{-}8)$$

Plasma arc power at the exit end of standoff column, $P_{3,o}$, absorbs Joule heating in standoff column, $P_{J,3}$, and subtracts radiative heat transfer loss in the same section, Q_s. Thus,

$$P_{3,o} = P_{3,i} + P_{J,3} - Q_s \qquad (5\text{-}9)$$

The corresponding plasma arc enthalpy at the exit end of standoff column is

$$h_{4,o} = \frac{P_{4,o}}{\dot{m}} \qquad (5\text{-}10)$$

(V-D) Plasma Arc Enthalpy Within Keyhole of Workpiece

Let us assume that entrance and exit ends of plasma arc enthalpy in the keyhole of workpiece are $h_{4,i}$ and $h_{4,o}$, respectively.

The plasma arc power, $P_{4,i}$, and enthalpy, $h_{4,i}$, at the entrance end of the keyhole of workpiece are identical to the plasma arc power, $P_{3,o}$, and enthalpy, $h_{3,o}$, at the exit end of standoff column, respectively. Thus,

$$\left.\begin{aligned} P_{4,i} &= P_{3,o} \\ h_{4,i} &= h_{3,o} \end{aligned}\right\} \qquad (5\text{-}11)$$

Plasma arc power at the exit end of the keyhole of workpiece, $P_{4,o}$, absorbs power from partial contribution made by workpiece anode and cathode drops, $(1-\psi)P_{w,2}$, and subtracts convective heat loss in keyhole, $Q_{w,c}$ and free electron power loss in keyhole, $Q_{w,e}$. Thus,

$$P_{4,o} = P_{4,i} + (1-\psi)P_{w,2} - Q_{w,c} - Q_{w,e} \qquad (5\text{-}12)$$

The corresponding plasma arc enthalpy at the exit end of the keyhole of workpiece is

$$h_{4,o} = \frac{P_{4,o}}{\dot{m}} \tag{5-13}$$

(V-E) Plasma Arc Enthalpy Discharged from the Workpiece

Plasma arc power, Q_{dis}, and enthalpy, h_{dis} discharged from the keyhole of workpiece is identical to the plasma arc power, $P_{4,o}$, and enthalpy, $h_{4,o}$, at the exit end of keyhole, namely

$$\left.\begin{aligned} Q_{dis} &= P_{4,o} \\ h_{dis} &= h_{4,o} \end{aligned}\right\} \tag{5-14}$$

Calculation of plasma arc enthalpy at each part of VPPA welding system will be illustrated in Section VIII of this report.

VI. Calculation of Crown and Root Bead Widths

Bead width is calculated from the heat absorbed in the workpiece, Q_W. As shown in Equation (4-15) Q_W is the summation of convection heating (The empirical relation actually includes radiation.) from the plasma, "direct" heating of the surface by current passing through localized surface voltage drops, and heat carried into the surface by hot electrons from the plasma.

For the purpose of estimating the melting isotherm surface of the weld puddle the total heat absorption Q_W is taken to enter the workpiece at a distance ϕL_4 above the bottom of the plate, where L_4 stands for the thickness of the workpiece, and ϕ represents a fraction of the thickness. If $\phi = 0.5$, the heat source is located at the center of the plate and the temperature distribution is symmetrical such that the puddle crown and root will be identical in size: an appropriate model for a full penetration keyholeing plasma arc weld. If $\phi > 0.5$, the heat source is located closer to the crown side of the plate and the crown will be wider than the root: a better model of a typical keyholeing weld. If $\phi = 1.0$, all the heat is delivered at the crown surface: a model suitable for representation of a GTA weld or a partial penetration VPPA weld. In the illustrative computations included in this report $\phi = 0.55$. By adjustment of ϕ it is possible to model effects of real assymetrical distributions of heating in the keyhole column as well as the further redistributions of heat due to circulations in the weld puddle and thus to model approximately the entire range of VPPA penetration phenomena.

The temperature field within the confined space between the two surfaces (assumed nonconducting) of the workpiece is constructed out of moving heat sources in an infinite continuum. "Image" sources are added outside the workpiece space so as to produce planes of symmetry across which no heat flows at the location of the workpiece surfaces. Given coordinate z zeroed at the bottom of the workpiece and extending up into the workpiece body and locating the heat source Q_W at $z = \phi L_4$, then an image heat source below the bottom of the plate of strength Q_W located at $z = \phi L_4$ creates a plane of zero heat flow at $z = 0$, the location of the bottom surface of the workpiece. The latter plane will remain and a further plane of zero heat flow at the site of the top surface of the workpiece will be created if an infinite array of image heat source pairs is constructed along the z-axis, each heat source pair of strength Q_W spaced at $\pm\phi L_4$ about an infinite array of points spaced at $2L_4$ and including $z = 0$.

The temperature T_c at location (x_c, y_c, z_c) within the workpiece due to the welding power input to the workpiece is then:

$$T_c - T_0 = \sum_{i=0}^{\infty} \frac{Q_W}{4\pi K R_i} \exp\left(-\frac{u(R_i + x_c)}{2\alpha}\right) \qquad (6\text{-}1)$$

where

T_0 = Ambient temperature of workpiece

K = Thermal conductivity of workpiece

u = Weld speed (in the x-direction)

α = Thermal diffusivity of workpiece

R_i = Distance between the i^{th} point heat source and the point of interest

R_i is computed as follows:

$$R_i = \sqrt{x_c^2 + y_c^2 + (z_i - z_c)^2} \qquad (6\text{-}2)$$

Weld bead width is determined by locating the largest value of y_c for which $T_c = T_\infty$, the melting temperature of the workpiece, at $z = 0$ (root) and $z_c = L_4$ (crown). The weld widths are twice the values of these y_c's. A converging computer search routine is used to make the computation.

Two approximations are used in the computations. First, the summation is truncated. 35 source points are used, 17 image sources on each side of the weld heat source. The values of z_i are generated by a recurrence relation:

$$z_i = z_{i-2} + 2L_4 \qquad (6\text{-}3)$$

where the starting values are:

$$z_1 = -16L_4 - \phi L_4 \qquad (6\text{-}4)$$

$$z_2 = -16L_4 + \phi L_4 \qquad (6\text{-}5)$$

An evaluation of the z_i's will show that z_{18} $(=\phi L_4)$ is the weld heat source located in the workpiece.

Second, although the maximum values of y_c on the melting isotherm occur somewhat behind $x_c = 0$, for the sake of a substantially easier compuation it is considered sufficiently accurate to accept for the maximum value of y_c the slightly (at the values of u appropriate to VPPA welding) smaller value of y_c that intersects the melting isotherm at $x_c = 0$ (Solomon and Levy, 1981; Tsai, 1982) satisfying the equation:

$$T_\infty - T_0 = \sum_{i=0}^{35} \frac{Q_w}{4\pi K R_i} \exp\left\{ - \frac{uR_i}{2\alpha} \right\} \qquad (6\text{-}6)$$

where

$$R_i = \sqrt{y_0^2 + (z_i - z_c)^2} \quad (6\text{-}7)$$

$$z_c = 0 \text{ for the root} \quad (6\text{-}8)$$

$$z_c = L_4 \text{ for the crown} \quad (6\text{-}9)$$

and the z_i are generated in accordance with Equations (6-3) to (6-5).

VII. Calculation of Crown and Root Heights

(VII-A) Volume Conservation Equation of Materials

Reinforcement profiles of crown and root beads are represented as paraboloids, as shown in Figure 4. Paraboloidal profiles can be expressed as a special case (where n=2) of the following equation:

$$Z = h\left[1 - \left(\frac{2y}{d}\right)^n\right] \qquad (7\text{-}1)$$

where

y = Distance from weld centerline

z = Local bead height

h = Maximum bead height

d = Bead width

n = Numerical value greater than 1

The cross-sectional area of the crown reinforcement is

$$A_c = 2\int_0^{d_c/2} \left\{ h_c\left[1 - \left(\frac{2y}{d_c}\right)^n\right]\right\} dy$$

$$= \frac{n}{n+1} h_c d_c$$

where

h_c = Crown height

d_c = Crown bead width

Similarly, cross-sectional area of the root reinforcement is

$$A_r = \frac{n}{n+1} h_r d_r$$

where

h_r = Root height

d_r = Root bead width

Volume conservation equation can be established based on the equilibrium relation between the material volume provided by welding wire and reinforcement volume enlargement of crown and root beads which is given by

$$\frac{n}{n+1} d_c h_c + \frac{n}{n+1} d_r h_r = \frac{\pi}{4} d_w^2 \frac{V_w}{u} - L_4 \cdot W_g \qquad (7\text{-}2)$$

where

d_w = Diameter of wire

V_w = Wire feed rate

u = Weld speed

W_g = Initial gap at weld seam

L_4 = Thickness of workpiece

(VII-B) Force Equilibrium Equation

For the purpose of deriving the force equilibrium equation, one has to calculate cross-sectional areas a, b, and c, defined in Figure 5, which are given by

$$A_a = 2 \int_0^{d_r/2} \left\{ h_c \left[1 - \left(\frac{2y}{d_c} \right)^n \right] \right\} dy$$

$$= h_c d_r - \frac{1}{n+1} h_c d_c \left(\frac{d_r}{d_c} \right)^{n+1} \qquad (7\text{-}3)$$

Similarly,

$$A_b = d_r \cdot L_4 \qquad (7\text{-}4)$$

and

$$A_c = A_r = \frac{n}{n+1} h_r d_r \tag{7-5}$$

Slopes at points B (crown) and D (root), shown in Figure 5, can be expressed as follows:

$$\tan \theta_c = \left.\frac{dz}{dy}\right|_{y=d_r/2} = -\frac{2nh_c}{d_c}\left(\frac{d_r}{d_c}\right)^{n-1}$$

and

$$\tan \theta_r = \left.\frac{dz}{dy}\right|_{y=d_r/2} = -\frac{2nh_r}{d_r}$$

With reference to the free-body diagram shown in Figure 5, one can derive the force equilibrium equation by the balancing of forces, which include gravitation, surface tension and pressure acting on the molten weld puddle:

$$\left[h_c d_r - \frac{1}{n+1} h_c d_c \left(\frac{d_r}{d_c}\right)^{n+1} + d_r \cdot L_4 + \frac{n}{n+1} d_r h_r\right] \rho g$$

$$= 4n\left[\frac{h_r}{d_r} - \frac{h_c}{d_c}\left(\frac{d_r}{d_c}\right)^{n-1}\right]\sigma - \bar{p}\, d_r \tag{7-6}$$

(VII-C) Calculation of Crown and Root Heights in Flat Welding (with Consideration of Gravity Force)

In comparison between the effects of external pressure $\bar{p}$ and surface tension force acting on the molten fluids of welding, experience suggests that the external pressure is much smaller than that of the surface tension force. Therefore, $\bar{p}$ will be ignored in the force equilibrium equation (7-6). Crown and root heights, thus, can be solved simultaneously from Equations (7-2) and (7-6) which are

given by the following expressions:

$$h_c = \frac{-\left[1 - \frac{4}{d_r^2}(n+1)\frac{\sigma}{\rho g}\right]\left[\frac{\pi}{4} d_w^2 \frac{V_w}{u} - L_4 \cdot W_g\right] - d_r \cdot L_4}{d_r - \frac{n}{n+1} d_c + \frac{4n\sigma}{\rho g}\left[\frac{1}{d_c}\left(\frac{d_r}{d_c}\right) + \frac{d_c}{d_r^2}\right] - \frac{1}{n+1} d_c \left(\frac{d_r}{d_c}\right)^{n+1}} \tag{7-7}$$

$$h_r = \frac{\frac{\pi}{4} d_w^2 \frac{V_w}{u} - L_4 \cdot Wg - \frac{n}{n+1} d_c h_c}{\frac{n}{n+1} d_r} \tag{7-8}$$

(VII-D) Calculation of Crown and Root Heights in Vertical Welding (Without Gravity Effect)

The effect of gravity force on the molten fluids of welding can be ignored for the case of vertical welding or the welding carried out at in space at zero-gravity. In this respect, one can ignore the terms of both gravity force and external pressure in Equation (6-6) which is given by

$$h_r = h_c \left(\frac{d_r}{d_c}\right)^n \tag{7-9}$$

Substituting this equation to Equation (7-2), on obtains

$$h_c = \frac{\frac{\pi}{4} d_w^2 \frac{V_w}{u} - L_4 \cdot W_g}{\frac{n}{n+1}\left[d_c + d_r \left(\frac{d_r}{d_c}\right)^n\right]} \tag{7-10}$$

(VI-E) Solidification of Crown Height

Figure 6(A) shows the configuration of the cross-section of a

puddle with the interface between liquid (molten metal) and solid metal. As solidification occurs interfaces between the molten and solid metals of the workpiece move together. Figure 6(B) shows the configuration of puddle with a trapezoid liquid-solid interfaces in contact at the just-completely solidified puddle root. It is postulated that the root solidifies before the crown because the root is farther from the heat source and, usually, the root is narrower. Figure 6(C) shows the configuration of the cross-section of the puddle after complete solidification. This figure shows shrinkage of the crown height that took place during solidification of the reservoir of molten metal above the frozen root. The cross-sectional area of the residual molten metal just after root solidification can be approximated as

$$A_c \simeq \frac{1}{2} L_4 \cdot d_c' \tag{7-11}$$

where L_4 stands for the thickness of the workpiece; and d_c', the crown width of the remaining reservoir of molten metal. Given specific volumetric shrinkage, $\Delta v/v$, of the metal during solidification a change of cross-sectional area of the remaining puddle molten zone takes place according to the followin relation:

$$\Delta A_c = A_c \left(\frac{\Delta v}{v}\right) = \frac{1}{2} L_4 \cdot d_c' \left(\frac{\Delta v}{v}\right) \tag{7-12}$$

From Equation (7-5) for the cross-sectional area of crown reinforcement, variation area of crown reinforcement can be shown as

$$\Delta A_c = \Delta \left(\frac{n}{n+1} d_c' h_c'\right) = \frac{n}{n+1} d_c' \Delta h_c' \tag{7-13}$$

Equating Equations (7-12) and (7-13) leads to

$$\frac{1}{2} L_4 \cdot d_c' \left(\frac{\Delta v}{v}\right) = \frac{n}{n+1} d_c' \Delta h_c'$$

or, simplifying, to

$$\Delta h_c' = \frac{n+1}{2n} L_4 \left(\frac{\Delta v}{v}\right) \qquad (7\text{-}14)$$

According to King (1987), the specific volumetric shrinkage for aluminum during the solidification, $\Delta v/v$, is 6.7%. Therefore, crown height shrinkage for aluminum during solidification can be expressed as

$$\Delta h_c' = 0.067 \frac{n+1}{2n} L_4 \qquad (7\text{-}15)$$

Detailed calculation results of crown and root heights are illustrated in Section VIII of this report.

VIII. Results of Computation

Recently, some limited experiments relating VPPA welding system parameters to voltage and bead configuration outputs have been carried out by General Digital Industries (GDI) through the sponsorship of NASA's Marshall Space Flight Center. Some of the input parameters used by GDI have been adopted in this study to permit comparison of the experimental observations made by GDI and our model computations. Tables 1 and 2 contain the basic input parameters to be adopted in the model computation. By using these input parameters, all the physical parameters listed for the VPPA welding system are computed.

Table 3 shows the electric potential illustrated in Figure 1 for standoff distances from 1 mm to 10 mm as computed by the model. All the symbols shown in the table are illustrated in the attached table of nomenclature.

Table 4 shows the itemized power inputs at various sections of VPPA welding system for standoff distances from 1 mm to 10 mm from model computation.

Table 5 shows plasma jet power, enthalpy and temperature profiles at various locations of VPPA welding system for standoff distances from 1 mm to 10 mm from model computations.

Table 6 shows power loss at various sections of the VPPA welding system for standoff distances from 1 mm to 10 mm from model computations. From this table we draw the following conclusions:

(a) Total electric power consumption increases as the standoff

distance increases;

(b) Power discharged from the outlet end of keyhole increases as the standoff distance increases while the percentage of the ratio of power discharged from the outlet end of the keyhole to total power consumption decreases as the standoff distance increases;

(c) Power absorbed by the workpiece, which melts metal and produces the weld, increases as the standoff distance increases as does the power discharged from the outlet end of keyhole;

(d) Power absorbed by the workpiece is less than the power discharged through the outlet end of keyhole;

(e) Power loss percentage in the gap between electrode and nozzle and at the nozzle both decrease as the standoff distance increases while the power loss percentage in the standoff column increases; and

(f) Plasma jet temperature at the outlet end of the keyhole ranges from 13700 to 14900 ^{0}K as the standoff distance varies from 1 mm to 10 mm.

Table 7 shows crown width, root width and average width of workpiece computed from the model computation.

In the GDI experimental data available to date welding wire effects were not yet included. Hence these effects were not included in our calculations.

Computed results of total power input, power discharged, workpiece power loss and standoff power loss for various standoff

distances from 1 mm to 10 mm are shown in Figure 7. Figure 8 shows computed results of percentages of standoff jet column power loss, workpiece power loss and plasma discharge power loss for standoff distances from 1 mm to 10 mm.

Comparisons between the results of model computations and experimental observations are shown from Figures 9 to 13. Figure 9 shows computed transferred arc voltage at straight polarity for standoff distances from 1 mm to 10 mm with experimental observations for comparison.

Figure 10 shows computed transferred arc voltage at reverse polarity for standoff distances from 1 to 10 mm, with experimental observations for comparison. Figures 11, 12, and 13 show computed crown width, root width, and average bead width, respectively, for standoff distances from 1 to 10 mm, in comparison with that of the experimental observation. These results shown in Figures 9 to 13 clearly indicate that the computed results are in excellent agreement with the experimental measurements.

IX. DISCUSSION AND CONCLUSION

The purpose of this study is to provide an algorithm for computing crown and root widths and crown and root heights of a VPPA weld bead to be used as a component in a VPPA welding control system.

The power distribution has been analyzed for the argon plasma gas working fluid in the VPPA welding process.

The input parameters used to check this model are listed in Tables 1 and 2. Some of the input parameters were provided by GDI.

In the GDI experimental data available to date welding wire effects were not yet included. Hence these effects were not included in the calculations. Figures 9 to 13 show clearly that computed results of transferred arc voltages at both straight and reverse polarities, and crown, root and average bead widths for standoff distances from 1 to 10 mm are so far in good agreement with the experimental measurements.

It must be remembered that the model as it stands now is not complete. For example, it remains to incorporate into the model the effect of surface tension gradient driven circulations, which are extremely sensitive to surface contamination levels of various sorts. Small differences in chemistry can result in great differences in puddle configuration and weld penetration (Lambert, 1991).

The most important and critical points for the model computations are that some physical parameters and their profiles, which are not measured by the experimental observations, can be shown and illustrated clearly from the mathematical computations. These

important physical parameters and their profiles include power input, power loss, enthalpy and temperature profiles and distributions at various sections of VPPA welding system. Also, what are the main causes and contributors to provide the mechanisms of power loss can only be disclosed from the model computation. These important physical mechanisms are illustrated in Tables 4 to 6 and Figures 7 and 8.

REFERENCES

Abramovich, G. N., "The Theory of Turbulent Jets", PP. 671, MIT Press, MA., 1963.

American Society for Metals Handbook Committee, "Metals Handbook," 9the Edition, Vol. 2, PP. 855, American Society for Metals, Metals Park, OH, 1979.

Cram, L. E., J. Physics, D; Applied Physics, 18, 401-411, 1985.

Drellishak, K. S., Knopp, C. F., and Cambell, A. B., "Partition Function and Thermodynamic Properties of Argon Plasma," AEDC-TDR-63-146, PP. 238, Arnold Engineering Development Center, TN, 1963.

Evans, D. L., and Tankin, R. S., Physics of Fluids, 10(6), 1137-1144, 1967.

Hsu, Y. T., and Rubinsky, B., "Transient Melting of a Metal Plate by a Penetrating Plasma Arc," J. Heat Transfer, 109, 463-469, 1987.

Ibele, W., "Modern Developments in Heat Transfer", PP. 443, Academic Press, New York, 1963.

King, F., "Aluminum and Its Alloys", pp. 313, The Camelot Press, Southampton, United Kingdom, 1987.

Lambert, J. A., "Cast-to-Cast Variability in Stainless Steel Mechanized GTA Welds", Welding Journal, 70(5), 41-52, 1991.

Lancaster, J. F., "The Physics of Welding", 2nd Edition, PP. 340, Pergamon Press, Oxford, England, 1986.

Metcalfe, J. C., and Quigley, A. B. C., "Heat Transfer in Plasma Arc Welding", Welding Journal, 54, 995-1035, 1975.

Miller, H. R., and Filipski, S. P., "Automated Plasma Arc Welding for Aerospace and Cryogenic Fabrication", Welding Journal, 45, 493-501, 1966.

Nunes, A. C., Jr., Modeling the VPPA Welding Process, Paper in Advanced Aerospace Materials/Process Conference, 1991a.

Nunes, A. C., Jr., Private Communication, 1991b.

Nunes, A. C., Jr., Novak, H. L. and McIlwain, M. C., "Weld Geometry Strength Effect in 2219-T87 Aluminum", NASA Technical Memorandum TM-82404, 1981.

Nunes, A. C., Jr., Bayless, O. E., Jr., Jones, C. S., III, Munafo, P. M., Biddle, A. P., and Wilson, W. A., "The Variable Polarity Plasma Arc Welding Process: Its Application to the Space Shuttle External Tank-First Interim Report", NASA Technical Memorandum TM-82532, 1983.

Nunes, A. C., Jr., Bayless, O. E., Jr., Jones, C. S., III, Munafo, P. M., Biddle, A. P., and Wilson, W. A., "Variable Polarity Plasma Arc Welding on the Space Shuttle External Tank", Welding Journal, 63, 27-35, 1984a.

Nunes, A. C., Jr., Bayless, O. E., Jr., Jones, C. S., III, Munafo, P. M., Biddle, A. P., and Wilson, W. A., "Variable Polarity Plasma Arc Welding Process: Its Application to the Space Shuttle External Tank-Second Interim Report", NASA Technical Memorandum TM-86482, 1984b.

O'Brien, R. L., "Arc Plasma for Joining, Cutting and Surfacing", Welding Research Council, No. 131, 1968.

Privozhik, L. J., and Miller, H. R., "Evaluation of Plasma Arc Welding

for 120 inch Diameter Rocket Motor Cases", Welding Journal, 45, 717-725, 1966.

Robert, C. W., and Melvin, J. A., "CRC Handbook of Chemistry and Physics", 61st Edition, CRC Press, NY, 1981.

Rosenthal, D., Welding Journal, 20, 220, 1941.

Tsai, C. L., "Modeling of Thermal Behaviors of Metal During Welding", in Trends in Welding Research in the United States, Edited by S. A. David, American Society for Metals, pp. 91-108, 1982.

FIGURE CAPTIONS

Figure 1. VPPA electric power system. The left side shows the straight polarity mode, and the right shows the reverse polarity mode.

Figure 2. Geometry and dimensions of the keyhole's approximate simplified heat transfer area.

Figure 3. Point heat source in workpiece and 17 image heat sources added above and below.

Figure 4. Dimensions of the weld puddle cross-section.

Figure 5. Free body diagram for the balance among external pressure P, surface tension force σ, and gravitational force g over an approximate weld puddle cross section.

Figure 6. Conjectured configuration of the puddle cross-section during solidification. (A) Fully molten cross-section before phase transition, (B) Partially molten cross-section just after freezing of the root; and (C) Completely solidified cross-section.

Figure 7. Plasma arc total power input, power discharged, workpiece power loss and standoff power loss in terms of various standoff distances from 1 to 10 mm.

Figure 8. Percentage of standoff power loss, workpiece power loss and plasma arc jet discharged power loss in terms of various standoff distances from 1 to 10 mm.

Figure 9. Computed and observed main arc straight polarity voltages in terms of various standoff distances from 1

Table 1 Basic Input Parameters (I)

Symbol	Description	Data Input
L_1	Distance between electrode and nozzle	1.143 mm
L_2	Vertical length of nozzle	3.378 mm
L_4	Thickness of workpiece	9.525 mm
L_E	Length of electrode	66 mm
D	Nozzle diameter	3.175 mm
D_E	Electrode diameter	3.9688 mm
K_E	Thermal conductivity of electrode	235 $W/m \cdot {}^0K$
$\dot{m}$	Argon gas mass flow rate	0.1028 g/s
ϕ_E	Electrode work function	2.6 V
ϕ_N	Nozzle work function	4.5 V
ϕ_w	Workpiece work function	4.2 V
ΔV_a	Anode potential drop	4.4 V
ΔV_c	Cathode potential drop	8.8 V
I_m^+	Main electric current in straight polarity	200 A
I_m^-	Main electric current in reverse polarity	200 A
I_p^+	Pilot electric current in straight polarity	25 A
I_p^-	Pilot electric current in reverse polarity	45 A
t_+	Time duration for straight polarity	19 ms
t_-	Time duration for reverse polarity	4 ms
$\frac{\Delta V}{\Delta L}$	Voltage drop per unit length	2 V/mm
T_E	Electrode temperature	2500 ^0K
T_N	Nozzle temperature	916 ^0K
T_0	Environment temperature; Initial temperature of workpiece	298 ^0K

Table 2 Basic Input Parmeters (II)

Symbol	Description	Data Input
h_N	Plasma enthalpy corresponding to nozzle wall temperature	0.3672 $\frac{kJ}{g}$
h_W	Plasma enthalpy corresponding to keyhole temperature	0.3672 $\frac{kJ}{g}$
ψ	Fraction of power loss due to anode and cathode drops	0.0
ϕ	Location of welding heat source from back of workpiece in fraction of plate thickness	0.55
u	Welding travel speed	3.387 $\frac{mm}{s}$
σ	Surface tension	0.865 $\frac{N}{m}$
d_W	Feed wire diameter	1.5748 mm
V_w	Wire feed speed	0.000 $\frac{mm}{s}$
W_g	Initial gap distance between weld surfaces to be joined	0.000 mm
k_w	Thermal conductivity of workpiece	0.13 $\frac{kw}{m \cdot {}^{o}K}$
Cp_w	Specific heat of workpiece	0.864 $\frac{kJ}{kg \cdot {}^{o}K}$
ρ_W	Density of workpiece	2650 kg/m^3
n	Exponent of reinforcement shape	2.0

Table 3 Computed Electric Potential

Standoff (mm)	1	2	3	4	5	6	7	8	9	10
V_E (V)	-8.6	-8.6	-8.6	-8.6	-8.6	-8.6	-8.6	-8.6	-8.6	-8.6
V_C (V)	-17.36	-19.36	-21.36	-23.36	-25.36	-27.36	-29.36	-31.36	-33.36	-35.36
V_G (V)	-10.6	-12.6	-14.6	-16.6	-18.6	-20.6	-22.6	-24.6	-26.6	-28.6
V_B (V)	-19.64	-21.64	-23.64	-25.64	-27.64	-29.64	-31.64	-33.64	-35.64	-37.64
V_D (V)	-8.46	-10.46	-12.46	-14.46	-16.46	-18.46	-20.46	-22.46	-24.46	-26.46
V_A (V)	-25.84	-27.84	-29.84	-31.84	-33.84	-35.84	-37.84	-39.84	-41.84	-43.84
ΔV_m^+ (V)	25.84	27.84	29.84	31.84	33.84	35.84	37.84	39.84	41.84	43.84
ΔV_p^+ (V)	17.39	17.39	17.39	17.39	17.39	17.39	17.39	17.39	17.39	17.39
V_E' (V)	16.08	16.08	16.08	16.08	16.08	16.08	16.08	16.08	16.08	16.08
V_C' (V)	24.84	26.84	28.84	30.84	32.84	34.84	36.84	38.84	40.84	42.84
V_G' (V)	18.08	20.08	22.08	24.08	26.08	28.08	30.08	32.08	34.08	36.08
V_B' (V)	27.12	29.12	31.12	33.12	35.12	37.12	39.12	41.12	43.12	45.12
V_D' (V)	26.98	28.98	30.98	32.98	34.98	36.98	38.98	40.98	42.98	44.98
V_A' (V)	34.12	36.12	38.12	40.12	42.12	44.12	46.12	48.12	50.12	52.12
ΔV_m^- (V)	34.12	36.12	38.12	40.12	42.12	44.12	46.12	48.12	50.12	52.12
ΔV_p^- (V)	-7.14	-7.14	-7.14	-7.14	-7.14	-7.14	-7.14	-7.14	-7.14	-7.14

Table 4 Computed Power Input

Standoff (mm)	1	2	3	4	5	6	7	8	9	10
P_E (W)	1341.1	1341.1	1341.1	1341.1	1341.1	1341.1	1341.1	1341.1	1341.1	1341.1
$P_{N,1}$ (W)	128.2	128.2	128.2	128.2	128.2	128.2	128.2	128.2	128.2	128.2
$P_{N,2}$ (W)	125.3	125.3	125.3	125.3	125.3	125.3	125.3	125.3	125.3	125.3
$P_{W,1}$ (W)	947.1	947.1	947.1	947.1	947.1	947.1	947.1	947.1	947.1	947.1
$P_{W,2}$ (W)	1033	1033	1033	1033	1033	1033	1033	1033	1033	1033
$P_{J,1}$ (W)	486.5	486.5	486.5	486.5	486.5	486.5	486.5	486.5	486.5	486.5
$P_{J,2}$ (W)	1298.4	1298.4	1298.4	1298.4	1298.4	1298.4	1298.4	1298.4	1298.4	1298.4
$P_{J,3}$ (W)	400	800	1200	1600	2000	2400	2800	3200	3600	4000
P_{Total} (W)	5759.6	6159.6	6559.6	6959.6	7359.6	7759.6	8159.6	8559.6	8959.6	9359.6

Table 5 Computed Plasma Arc Jet Power, Enthalpy and Temperature

Standoff (mm)	1	2	3	4	5	6	7	8	9	10
$P_{1,i}$ (W)	1244.1	1244.1	1244.1	1244.1	1244.1	1244.1	1244.1	1244.1	1244.1	1244.1
$h_{1,i}$ (kJ/g)	12.1	12.1	12.1	12.1	12.1	12.1	12.1	12.1	12.1	12.1
$T_{1,i}$ (°K)	12046	12046	12046	12046	12046	12046	12046	12046	12046	12046
$P_{1,o};P_{2,i}$ (W)	1713.5	1713.5	1713.5	1713.5	1713.5	1713.5	1713.5	1713.5	1713.5	1713.5
$h_{1,o};h_{2,i}$ (kJ/g)	16.67	16.67	16.67	16.67	16.67	16.67	16.67	16.67	16.67	16.67
$T_{1,o};T_{2,i}$ (°K)	12813	12813	12813	12813	12813	12813	12813	12813	12813	12813
$P_{2,o};P_{3,i}$ (W)	2389.6	2389.6	2389.6	2389.6	2389.6	2389.6	2389.6	2389.6	2389.6	2389.6
$h_{2,o};h_{3,i}$ (kJ/g)	23.25	23.25	23.25	23.25	23.25	23.25	23.25	23.25	23.25	23.25
$T_{2,o};T_{3,i}$ (°K)	13655	13655	13655	13655	13655	13655	13655	13655	13655	13655
$P_{3,o};P_{4,i}$ (W)	2720.3	3027.4	3310.5	3570.4	3807.6	4024.5	4222.4	4404.0	4574.2	4727.8
$h_{3,o};h_{4,i}$ (kJ/g)	26.46	29.45	32.20	34.73	37.04	39.15	41.07	42.84	44.50	45.99
$T_{3,o};T_{4,i}$ (°K)	14035	14353	14646	14915	15182	15435	15667	15880	16115	16375
$P_{4,o}$ (W)	2458.8	2660.1	2837.2	2996.6	3134.2	3254.3	3351.7	3435.0	3502.1	3559.2
$h_{4,o}$ (kJ/g)	23.92	25.88	27.60	29.15	30.49	31.66	32.60	33.41	34.07	34.62
$_{4,o}$ (°K)	13735	13970	14156	14321	14464	14588	14689	14775	14844	14903

Table 7 Computed Bead Widths

Standoff (mm)	1	2	3	4	5	6	7	8	9	10
Crown Width (mm)	7.0	7.77	8.54	9.27	9.96	10.66	11.37	12.03	12.76	13.43
Root Width (mm)	4.39	5.59	6.68	7.63	8.53	9.37	10.20	11.01	11.82	12.57
Average Width (mm)	5.695	6.68	7.61	8.45	9.245	10.015	10.785	11.52	12.29	13.0

Table 6 Computed Power Loss

Standoff(mm)	1	2	3	4	5	6	7	8	9	10
Q_E (W)	97.0	97.0	97.0	97.0	97.0	97.0	97.0	97.0	97.0	97.0
Q_E/Q_{Total}	1.7%	1.6%	1.5%	1.4%	1.3%	1.3%	1.2%	1.1%	1.1%	1.0%
Q_G (W)	17.2	17.2	17.2	17.2	17.2	17.2	17.2	17.2	17.2	17.2
Q_G/Q_{Total}	0.3%	0.3%	0.3%	0.2%	0.2%	0.2%	0.2%	0.2%	0.2%	0.2%
Q_N (W)	875.7	875.7	875.7	875.7	875.7	875.7	875.7	875.7	875.7	875.7
Q_N/Q_{total}	15.2%	14.2%	13.3%	12.6%	11.9%	11.3%	10.7%	10.2%	9.8%	9.4%
Q_S (W)	69.3	162.2	279.1	419.3	582.1	765.1	967.3	1185.6	1415.4	1661.8
Q_S/Q_{Total}	1.2%	2.6%	4.3%	6.0%	7.9%	9.9%	11.9%	13.9%	15.8%	17.8%
Q_W (W)	2241.7	2347.4	2453.5	2553.9	2653.5	2750.3	2850.8	2949.2	3052.2	3148.8
Q_W/Q_{Total}	38.9%	38.1%	37.4%	36.7%	36.1%	35.4%	34.9%	34.5%	34.1%	33.6%
Q_{dis} (W)	2458.8	2660.1	2837.2	2996.6	3134.2	3254.3	3351.7	3435.0	3502.1	3559.2
Q_{dis}/Q_{Total}	42.7%	43.2%	43.3%	43.1%	42.6%	41.9%	41.1%	40.0%	39.1%	38.0%
Q_{Total} (W)	5759.6	6159.6	6559.6	6959.6	7359.6	7759.6	8159.6	8559.6	8959.6	9359.6

FIGURE CAPTIONS

Figure 1. VPPA electric power system. The left side shows the straight polarity mode, and the right shows reverse polarity mode.

Figure 2. Ring-shaped geometry and dimensions of the keyhole's simplified heat transfer area.

Figure 3. Distribution of real point heat sources in workpiece and 17 points each of heat sources added to the mirror reflection corresponding image point sources at upper and lower planes

Figure 4. Geometric coordinate of the weld puddle cross-section.

Figure 5. Free body diagram and the geometry of coordinate to describe the balance among external pressure P, surface tension force σ, and gravitational force g.

Figure 6. Configuration of the puddle cross-section with the liquid (molten metal)-solid metal. (A) Molten state puddle before phase transition, (B) Molten state puddle in the process of phase transition from molten metal to solidified metal; and (C) solidified metal of welding puddle.

Figure 7. Plasma arc total power input, power discharged, workpiece power loss and standoff power loss in terms of various standoff distances from 1 to 10 mm.

Figure 8. Percentage of standoff power loss, workpiece power loss and plasma arc jet discharged power loss in terms of

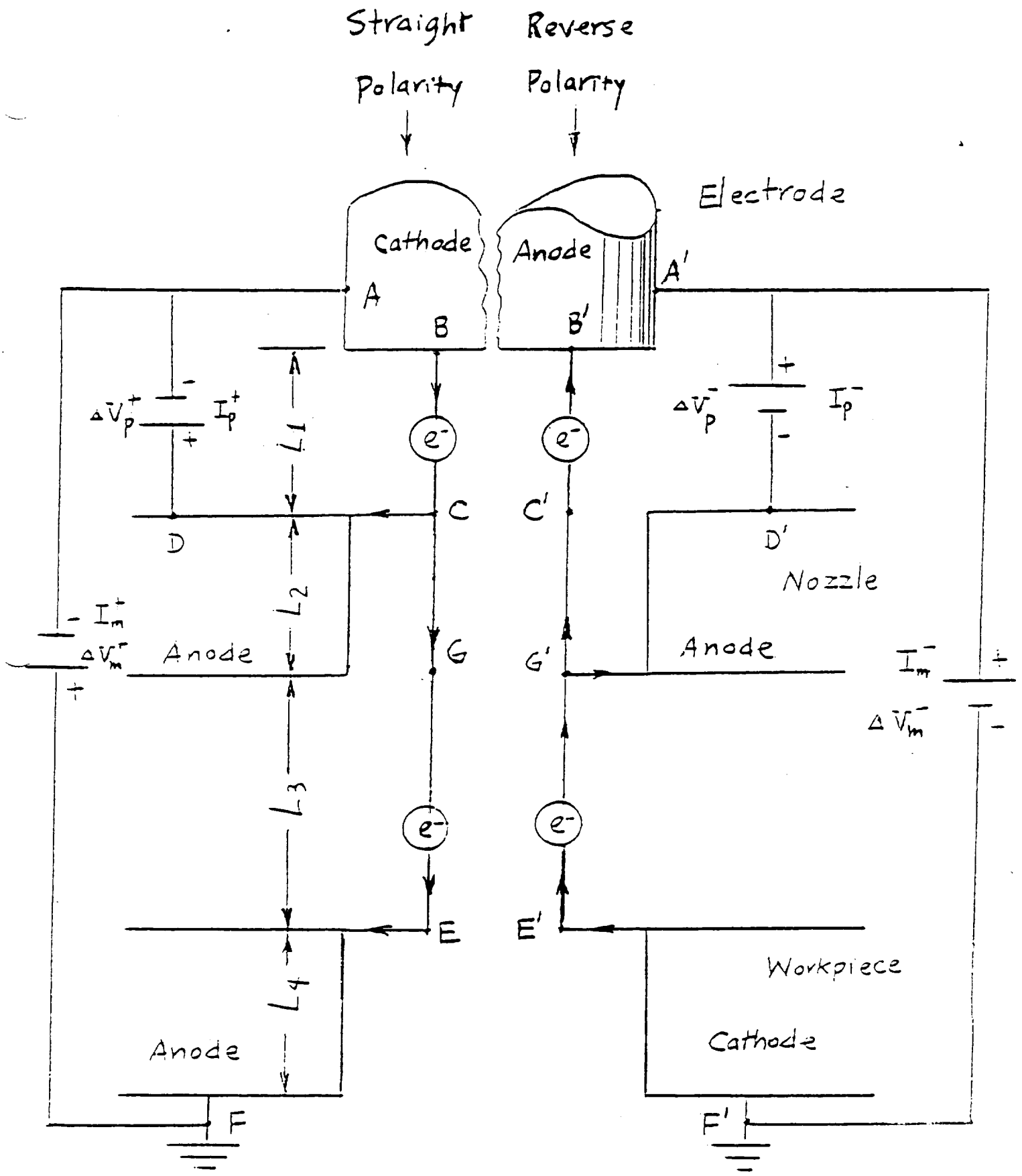
Straight Polarity
Reverse Polarity
Electrode
Cathode
Anode
A
A'
B
B'
ΔV_p^+
I_p^+
L_1
e^-
ΔV_p^-
I_p^-
C
C'
D
D'
Nozzle
I_m^+
ΔV_m^+
L_2
Anode
G
G'
Anode
I_m^-
ΔV_m^-
L_3
E
E'
Workpiece
L_4
Anode
Cathode
F
F'

Fig. 1

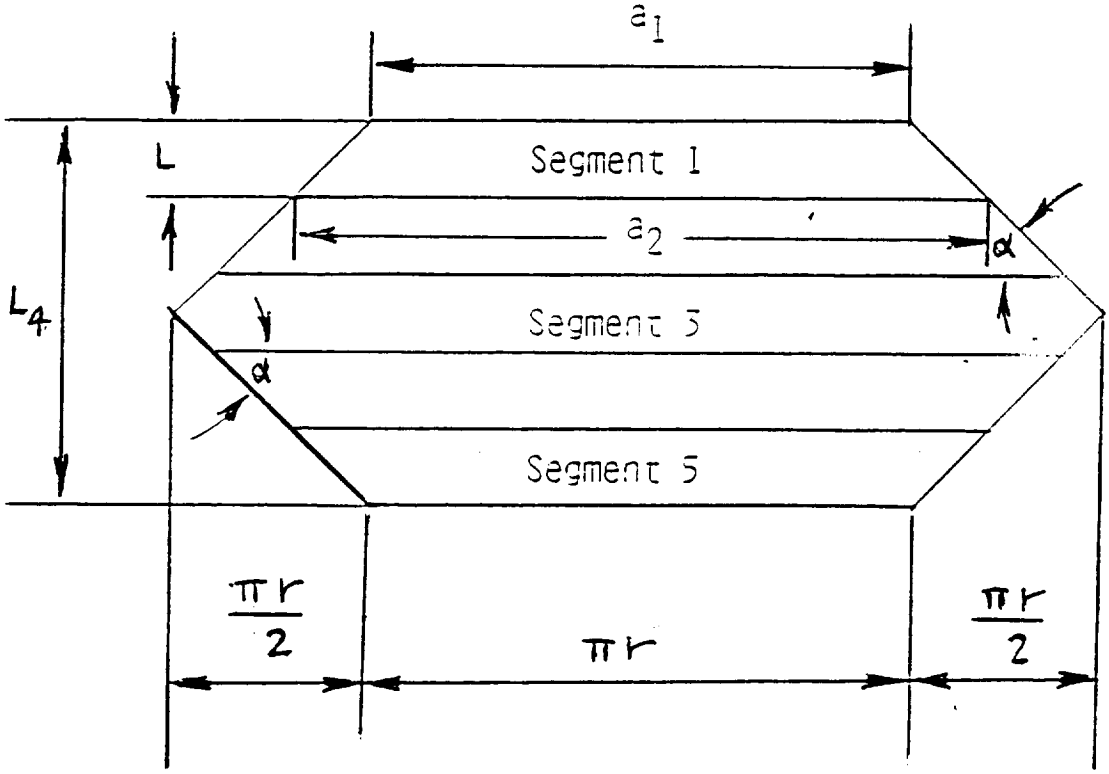

$$L = \frac{L_4}{5}$$

Fig. 2

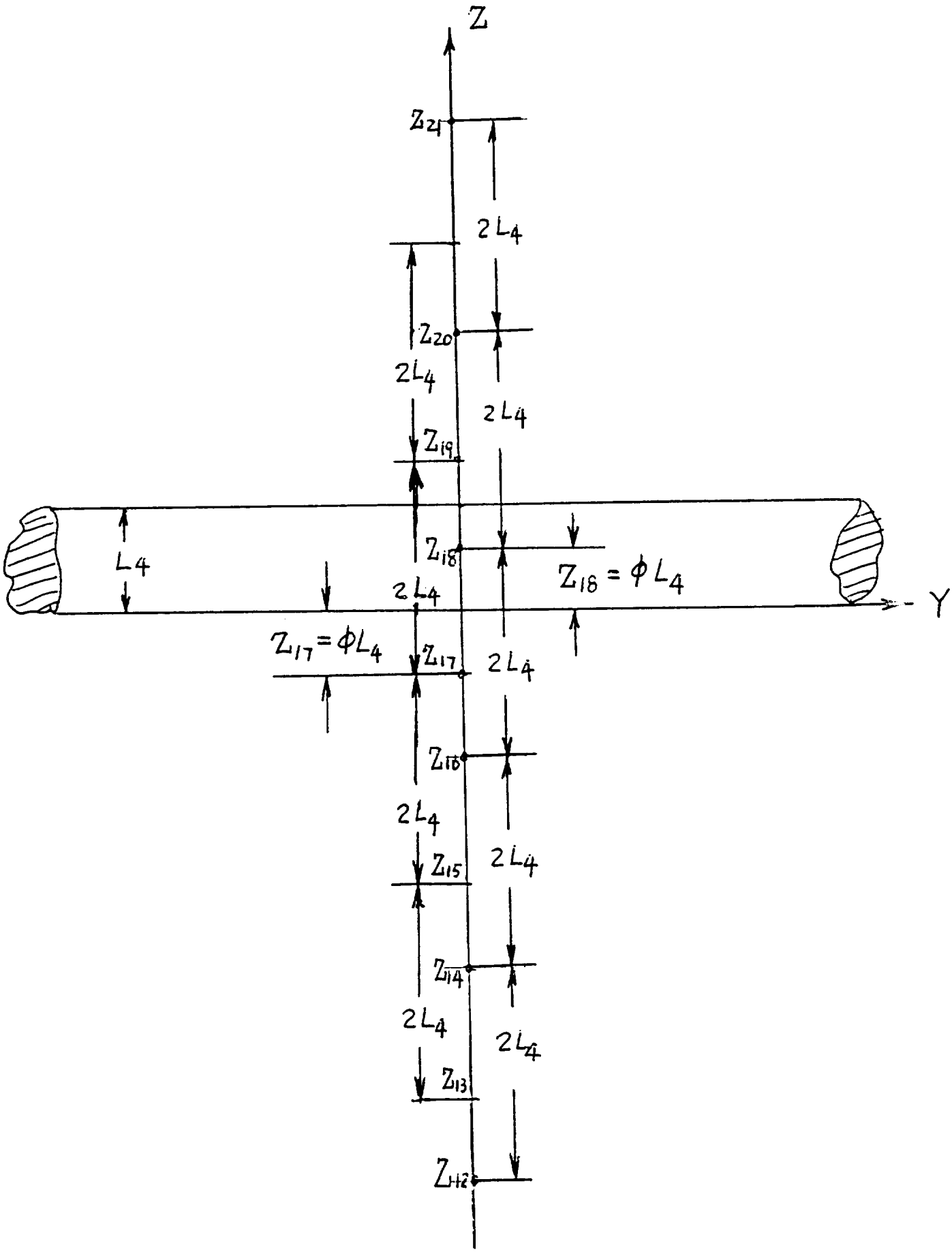
Z
Z21
2L4
Z20
2L4
2L4
Z19
Z18
L4
Z18 = ϕL4
2L4
Y
Z17 = ϕL4
Z17
2L4
Z16
2L4
2L4
Z15
Z14
2L4
2L4
Z13
Z12

Fig. 3

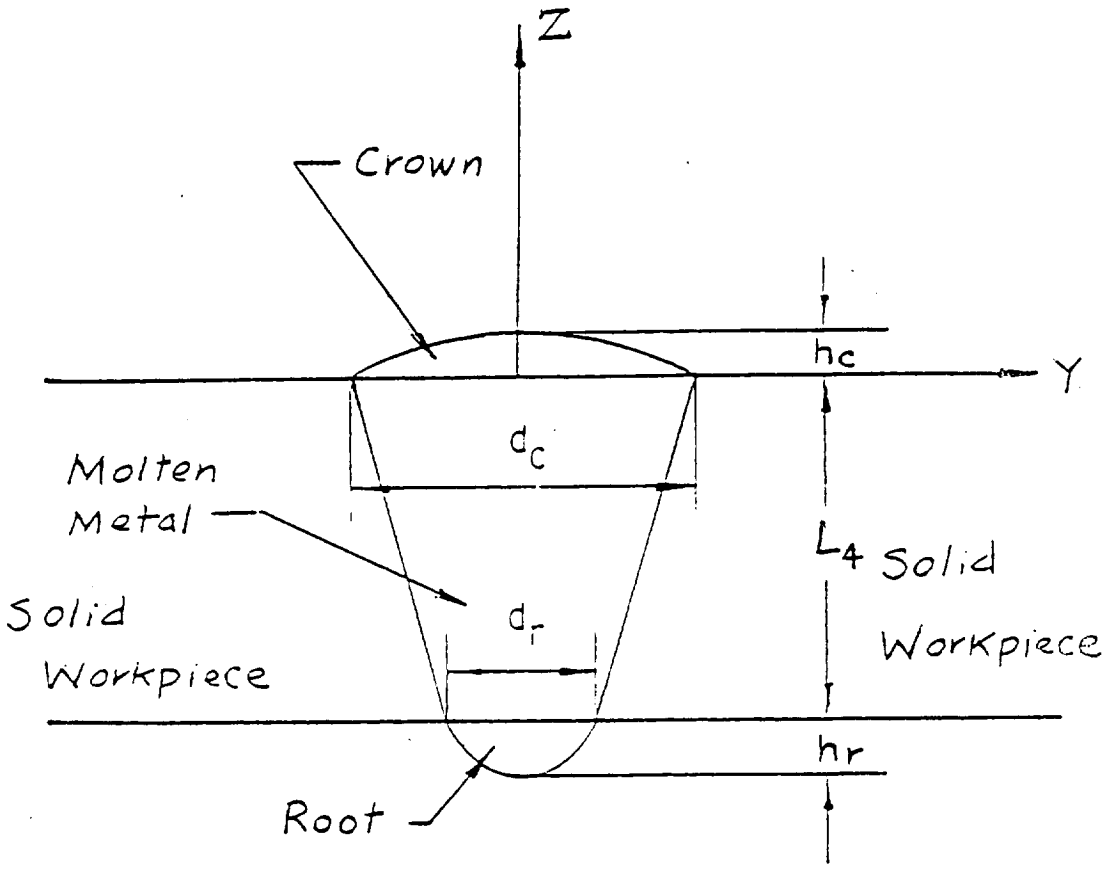
Z
Crown
hc
Y
dc
Molten
Metal
L4 Solid
Workpiece
Solid
Workpiece
dr
hr
Root

Fig. 4

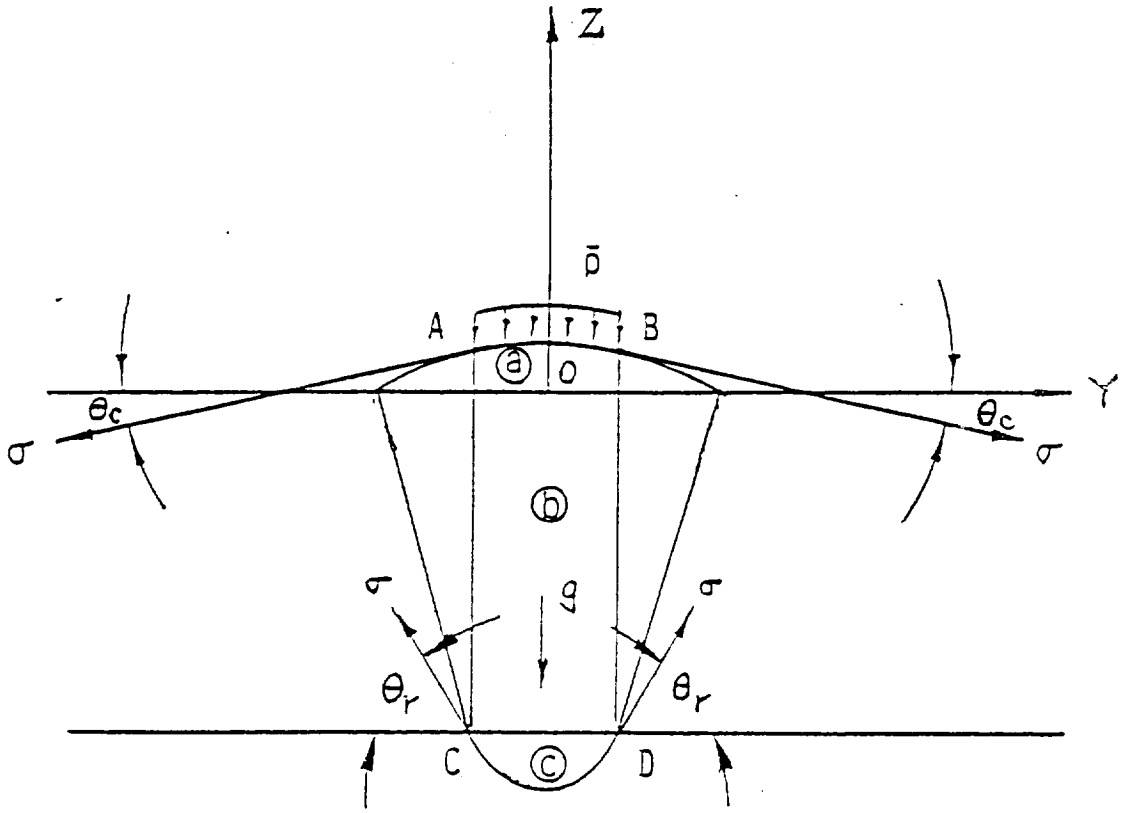

Fig. 5

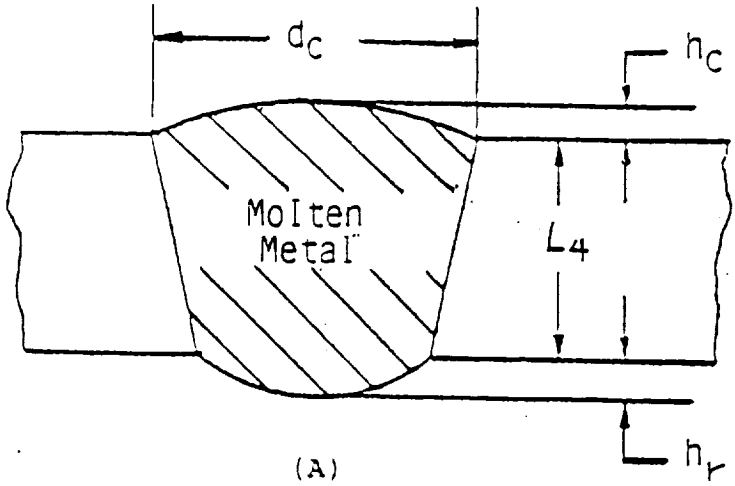

(A)

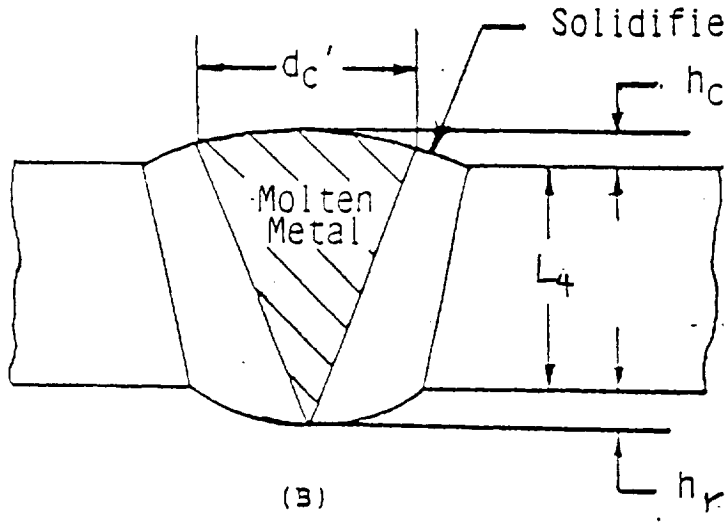

(B)

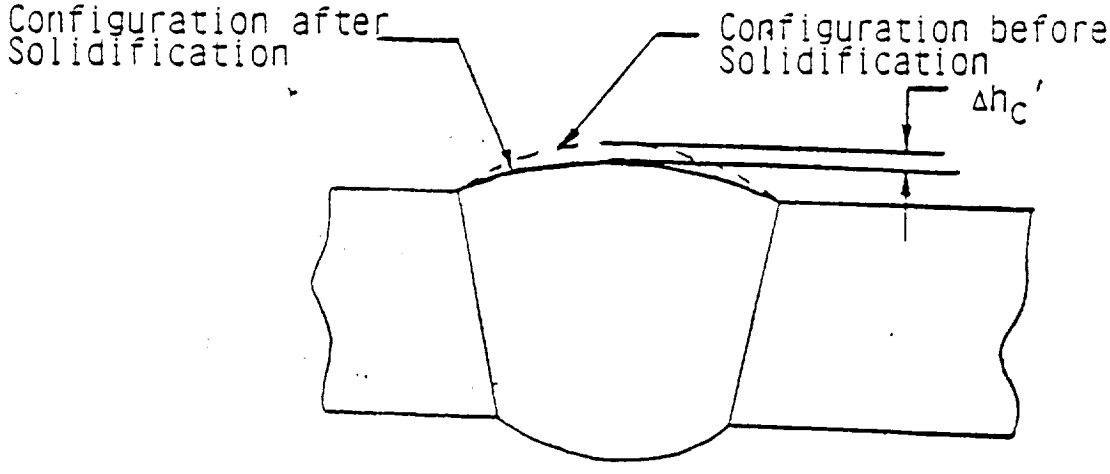

(C)

Figure 6 (A, B, C)

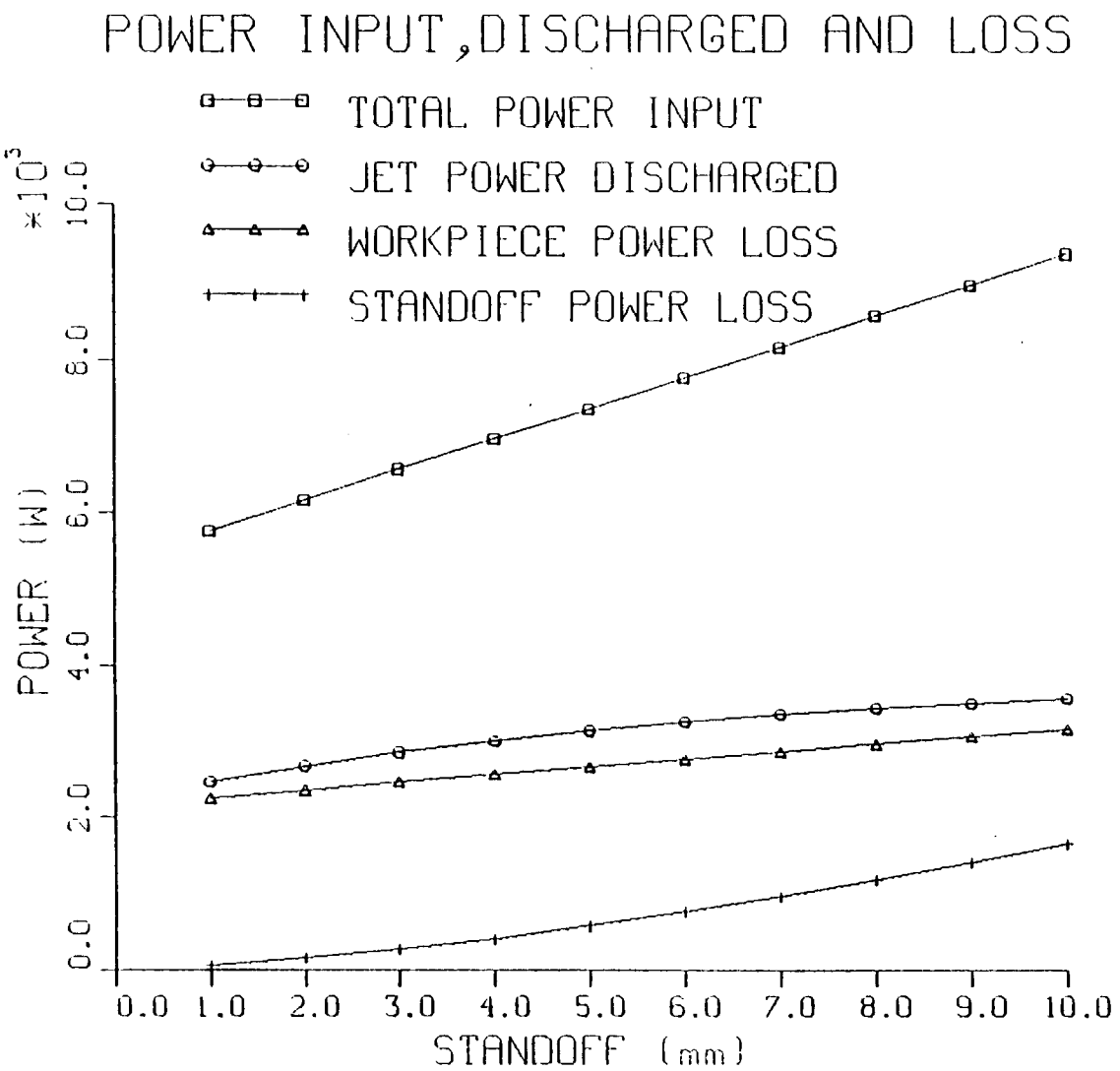
POWER INPUT,DISCHARGED AND LOSS
TOTAL POWER INPUT
JET POWER DISCHARGED
WORKPIECE POWER LOSS
STANDOFF POWER LOSS
POWER (W)
*10^3
0.0
2.0
4.0
6.0
8.0
10.0
0.0
1.0
2.0
3.0
4.0
5.0
6.0
7.0
8.0
9.0
10.0
STANDOFF (mm)

Fig. 7

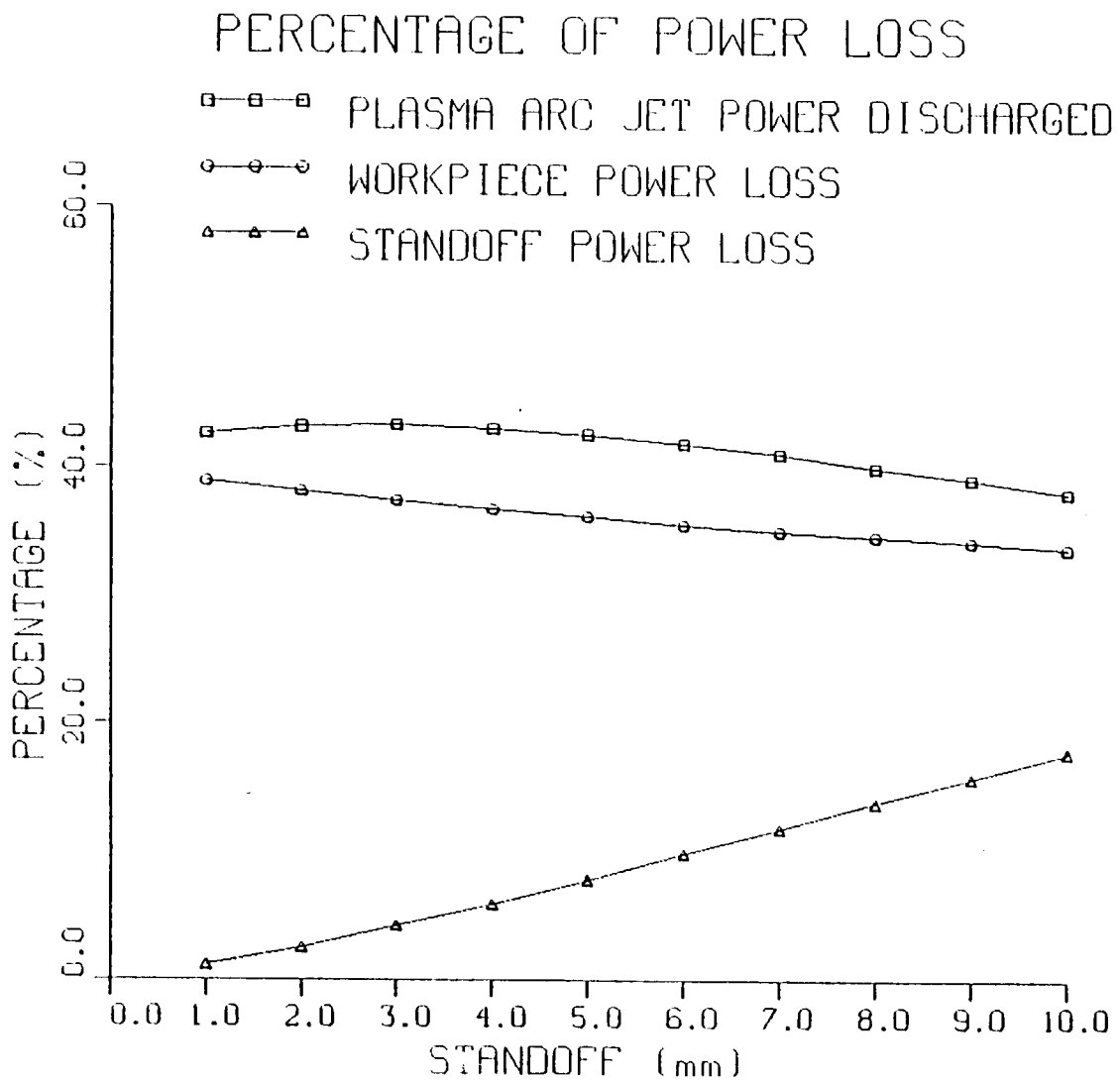
PERCENTAGE OF POWER LOSS
PLASMA ARC JET POWER DISCHARGED
WORKPIECE POWER LOSS
STANDOFF POWER LOSS
PERCENTAGE (%)
60.0
40.0
20.0
0.0
0.0 1.0 2.0 3.0 4.0 5.0 6.0 7.0 8.0 9.0 10.0
STANDOFF (mm)

Fig. 8

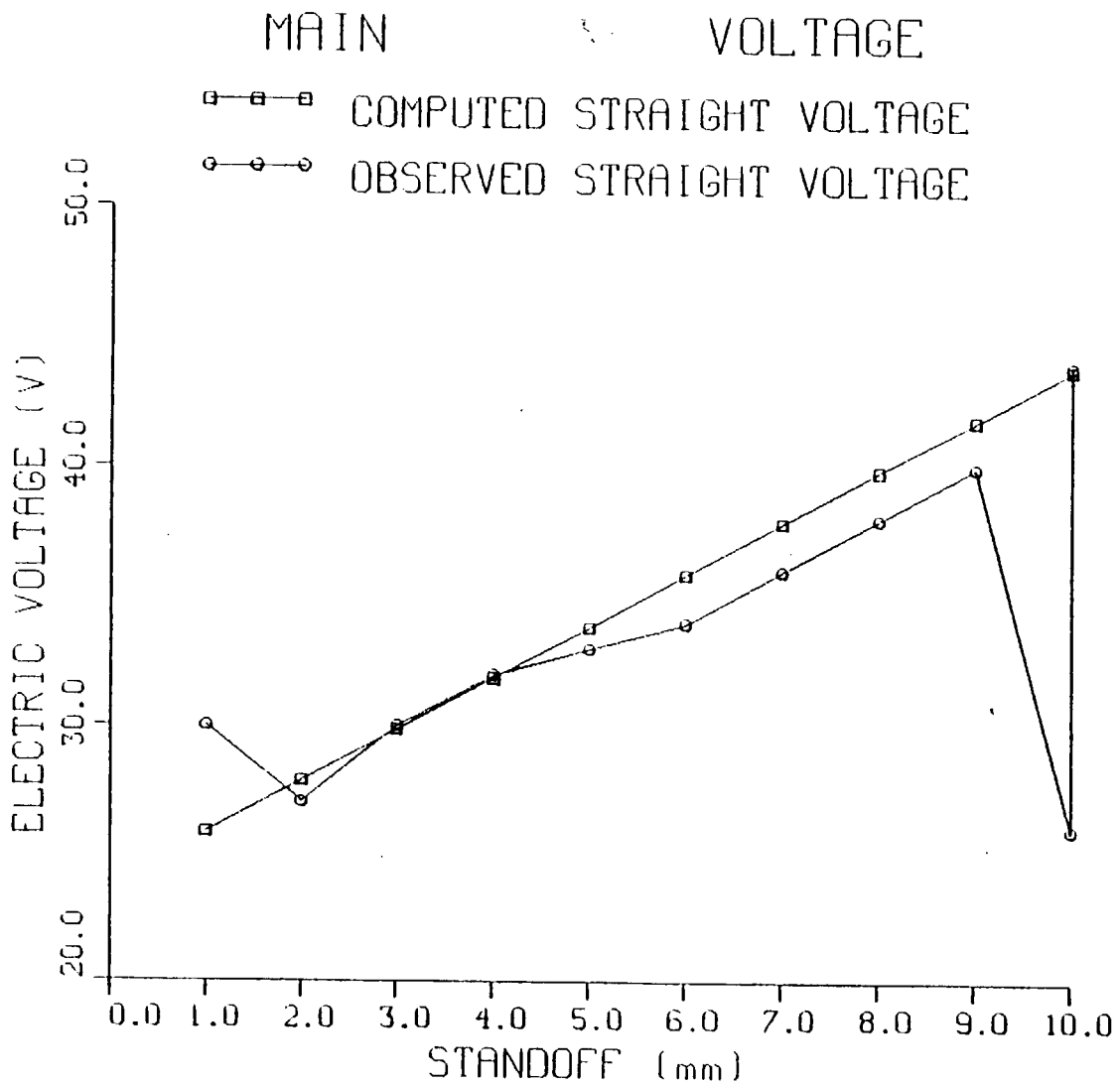
MAIN VOLTAGE
COMPUTED STRAIGHT VOLTAGE
OBSERVED STRAIGHT VOLTAGE
ELECTRIC VOLTAGE (V)
50.0
40.0
30.0
20.0
0.0
1.0
2.0
3.0
4.0
5.0
6.0
7.0
8.0
9.0
10.0
STANDOFF (mm)

Fig. 9

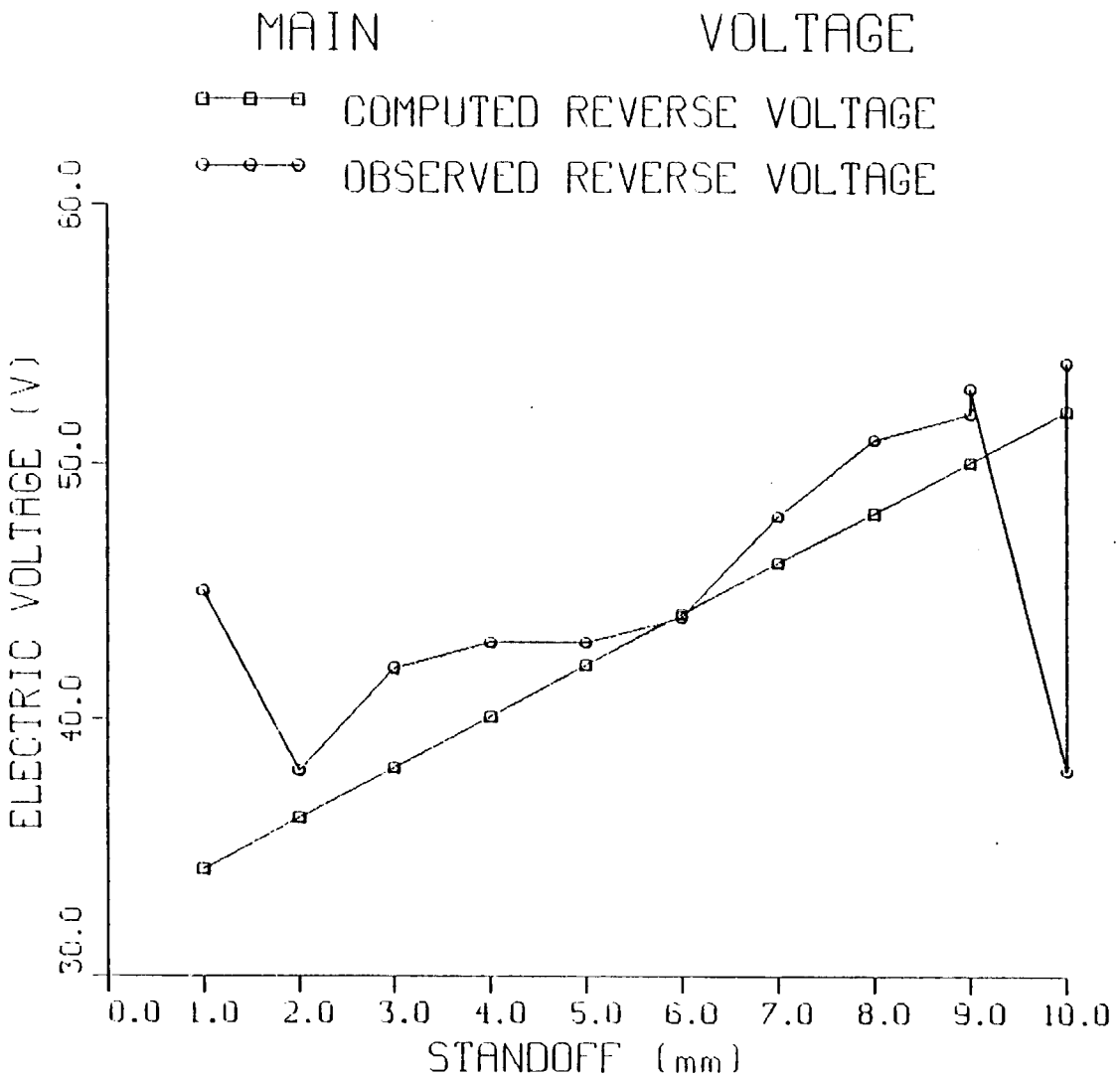
MAIN VOLTAGE
COMPUTED REVERSE VOLTAGE
OBSERVED REVERSE VOLTAGE
ELECTRIC VOLTAGE (V)
60.0
50.0
40.0
30.0
0.0
1.0
2.0
3.0
4.0
5.0
6.0
7.0
8.0
9.0
10.0
STANDOFF (mm)

Fig. 10

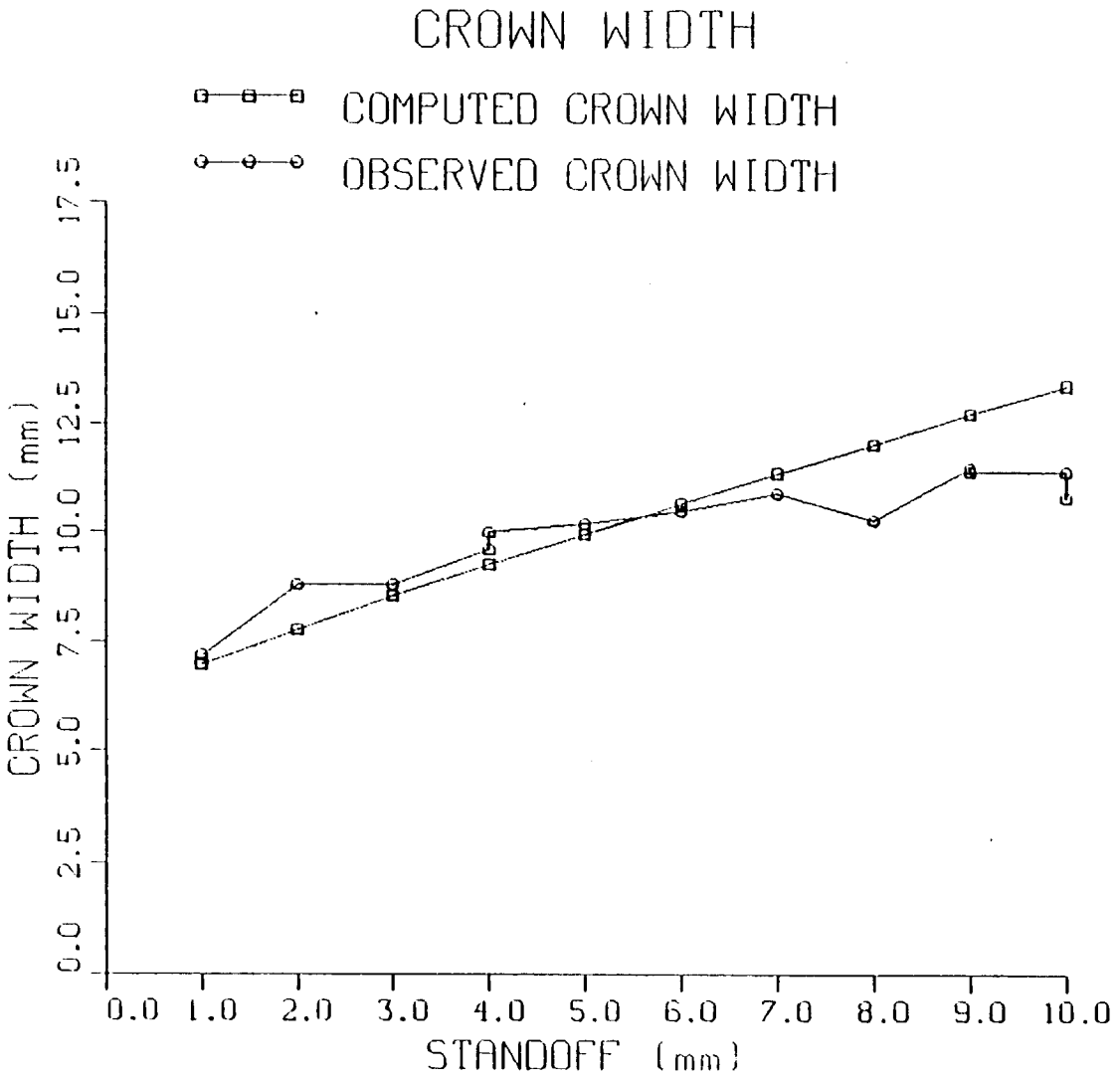
CROWN WIDTH
COMPUTED CROWN WIDTH
OBSERVED CROWN WIDTH
CROWN WIDTH (mm)
0.0
2.5
5.0
7.5
10.0
12.5
15.0
17.5
0.0
1.0
2.0
3.0
4.0
5.0
6.0
7.0
8.0
9.0
10.0
STANDOFF (mm)

Fig. 11

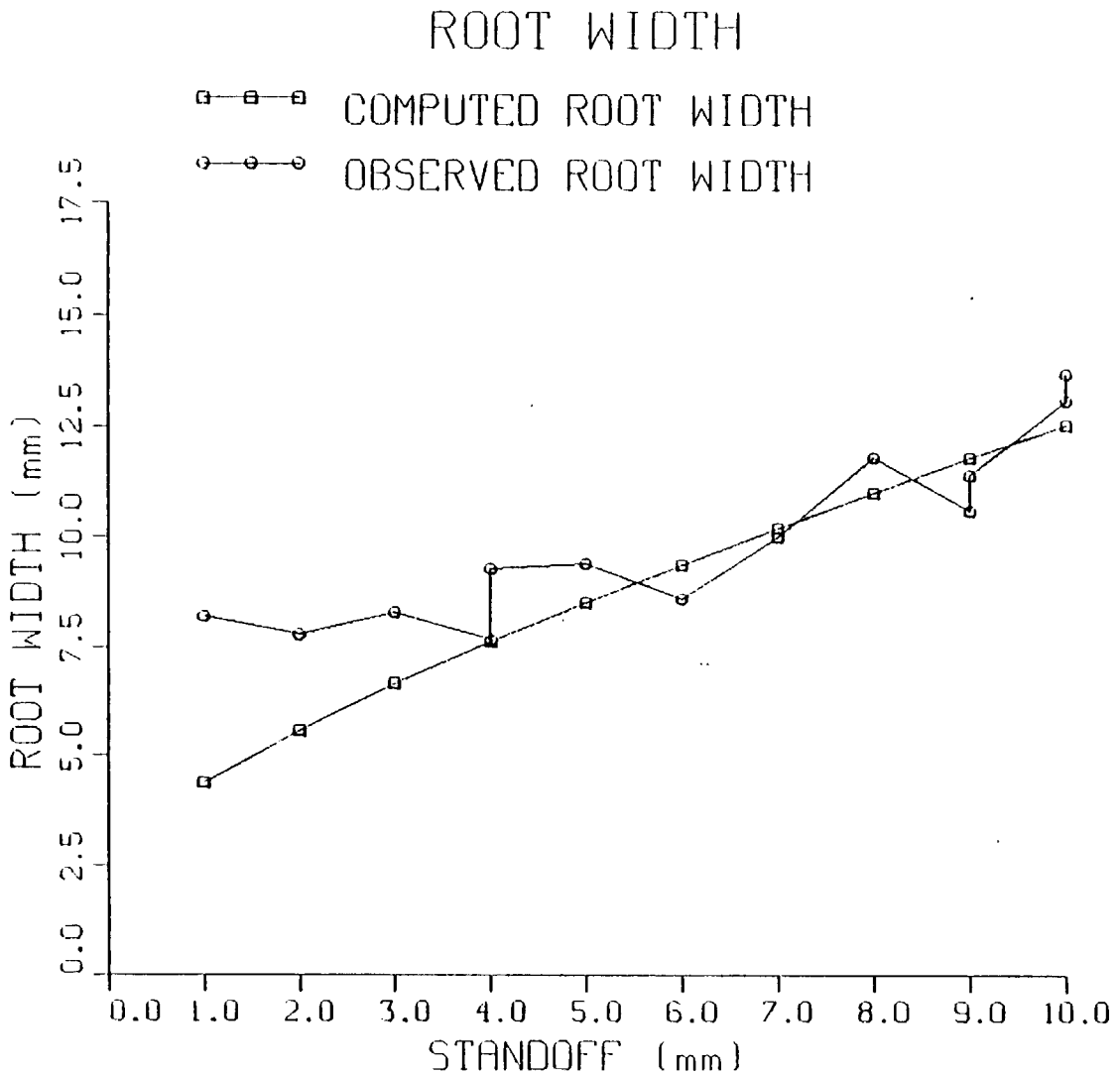
ROOT WIDTH
COMPUTED ROOT WIDTH
OBSERVED ROOT WIDTH
ROOT WIDTH (mm)
0.0
2.5
5.0
7.5
10.0
12.5
15.0
17.5
0.0
1.0
2.0
3.0
4.0
5.0
6.0
7.0
8.0
9.0
10.0
STANDOFF (mm)

Fig. 12

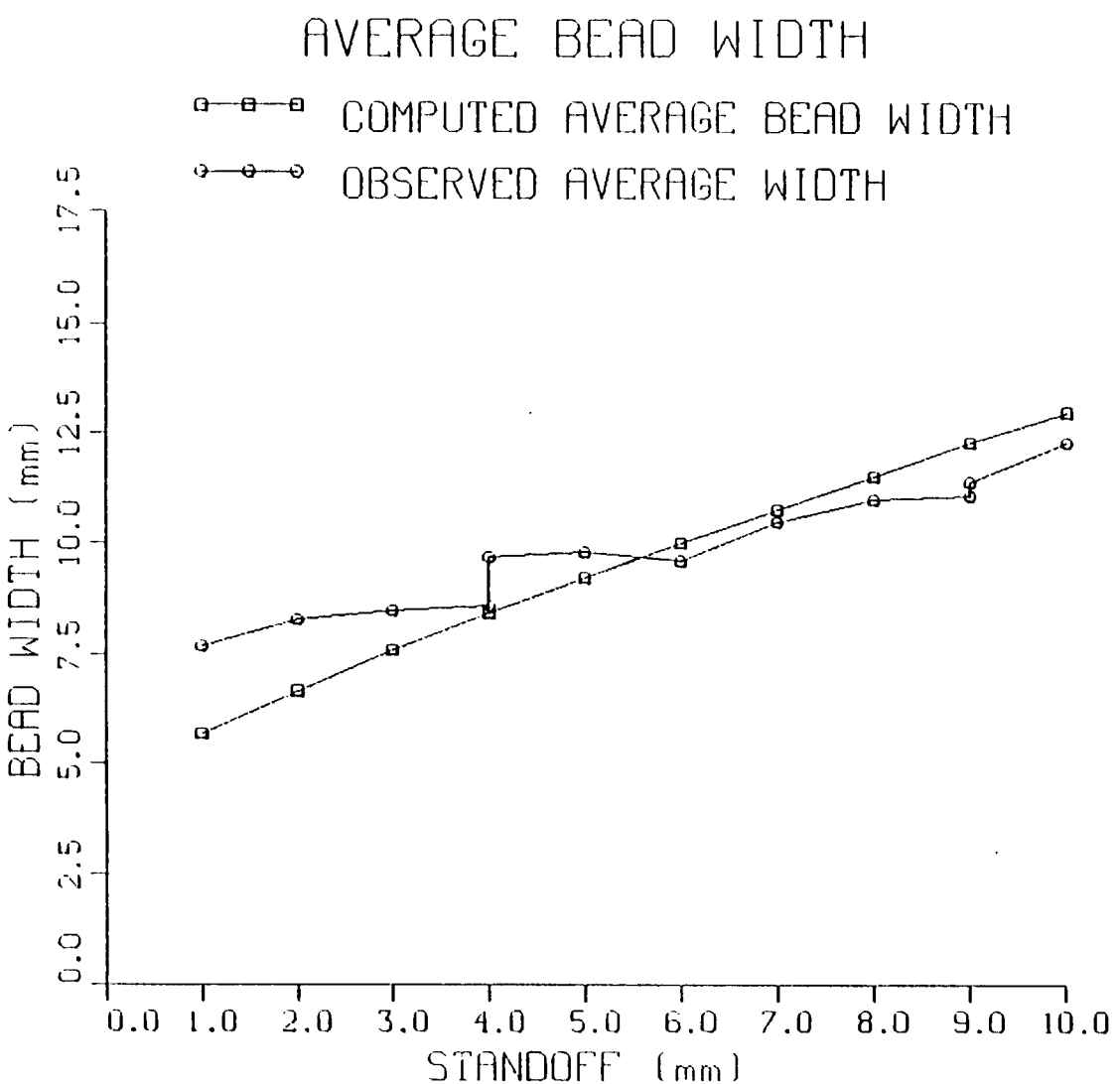

Fig. 13

NASA—MSFC—C